Title
Controlling magnetization and strain at the micron-scale and below in strain-mediated composite multiferroic devices

Author
Xiao, Zhuyun

Publication Date
2017

Peer reviewed|Thesis/dissertation

UNIVERSITY OF CALIFORNIA

Los Angeles

Controlling magnetization and strain at the micron-scale and below in strain-mediated composite multiferroic devices

A thesis submitted in partial satisfaction

of the requirements for the degree Master of Science

in Electrical Engineering

by

Zhuyun Xiao

2017

ABSTRACT OF THE THESIS

Controlling magnetization and strain at the micron-scale and below in strain-mediated composite multiferroic systems

by

Zhuyun Xiao

Master of Science in Electrical Engineering

University of California, Los Angeles, 2017

Professor Robert N. Candler, Chair

Strain-coupled multiferroic heterostructures provide a path to energy-efficient, voltage-controlled magnetic nanoscale devices, a region where current-based methods of magnetic control suffer from Ohmic dissipation. Magnetoelectric coupling behavior in such composite heterostructures has thus been of substantial interest for scientific research and applications. As the dimension of the devices scale down, novel physical phenomenon emerges and thus also requires further understanding of both the magnetization and strain behavior at micro- and nanoscale.

When it comes to the magnetization behavior, there has been a growing interest in highly magnetoelastic materials, such as Terfenol-D, prompting a more accurate understanding of their magnetization behavior. To address this need, we simulate the strain-induced magnetization change with two modeling methods: the commonly used unidirectional model and the recently developed bidirectional model. Unidirectional models account for magnetoelastic effects only, while bidirectional models account for both magnetoelastic and magnetostrictive effects. We found unidirectional models are on par with bidirectional models when describing the magnetic behavior in weakly magnetoelastic materials (e.g., Nickel), but the two models deviate when highly magnetoelastic materials (e.g., Terfenol-D)

are introduced. These results suggest that magnetostrictive feedback is critical for modeling highly magnetoelastic materials, as opposed to weaker magnetoelastic materials, where we observe only minor differences between the two methods' outputs. To our best knowledge, this work represents the first comparison of unidirectional and bidirectional modeling in composite multiferroic systems, demonstrating that back-coupling of magnetization to strain can inhibit formation and rotation of magnetic states, highlighting the need to revisit the assumption that unidirectional modeling always captures the necessary physics in strain-mediated multiferroics.

In terms of the strain behavior, there hasn't been a system-level work that quantifies the strain distribution as a function of the electric field at these so-called mesocales level (100 nm- 10 um), in the range of the constitutive grain size, etc. To obtain mechanical properties at such length scale, including strain information, we used synchrotron polychromatic scanning x-ray diffraction (micro-diffraction) on beamline 12.3.2 at the Advanced Light Source of the Lawrence Berkeley National Lab.

With given ferromagnetic and ferroelectric components, it is the magnetoelectric coupling between the two that governs the interaction. In this work, we also demonstrate a method to enhance the coupling behavior between two existing components by interposing a polymer layer.

The thesis of Zhuyun Xiao is approved.

Chandrashekhar J. Joshi

Chee Wei Wong

Oscar M. Stafsudd

Robert N. Candler, Committee Chair

University of California, Los Angeles

2017

TABLE OF CONTENTS

LIST OF FIGURES

ACKNOWLEDGEMENTS

It has been a wonderful experience to have my master's studies in the Sensor and Technology Laboratory at UCLA. I have received numerous help from many people to make the work possible. I would like to express my special thanks of gratitude to my advisor, Professor Robert N. Candler, for his professional guidance and valuable support throughout this work.

I also would like to express my gratitude Professor Chan J. Joshi, Professor Chee Wei Wong and Professor Oscar M. Stafsudd for serving as my thesis committee members and giving me insightful comments and advice that greatly help me improve my work. It is a great honor for me to have them serve as my thesis committee.

In addition, I would like to thank Center for Translational Applications of Nanoscale Multiferroic Systems (TANMS) at UCLA, funded by National Science Foundation, for the financial and knowledge support. I am deeply grateful to my outstanding collaborators for their indispensable support and contribution to my research work. In particular, I would like to thank Dr. Roberto Lo Conte at UC Berkeley, who had many helpful discussions with me regarding this work. It is my great pleasure to work with many other talented researchers from multidiscipline. I appreciate the the modeling support from Dr. Cheng-Yen Liang and Cai Chen at UCLA, the material support from Professor Greg Carman and Dr. Kotekar P. Mohanchandra at UCLA, Professor Sarah Tolbert and C. Ty Karaba at UCLA, and Rachel Steinhardt at Cornell University, and fabrication guidance from Hyunmin Sohn and Sidhant Tiwari.

I would like to thank Minji Zhu, the lab manager of the Center for High Frequency Electronics (CHFE) at UCLA, for his kind collaborations and support, and Dr. Yuwei Fan, the electron-beam lithography staff for her kind support and guidance. I would also like to

thank Dr. Andreas Scholl and Dr. Camelia Stan at Advanced Light Source, Lawrence Berkeley National Laboratory for their instructive technical advice.

Finally, I express my deepest love and special gratitude to my family for their unconditional love, encouragement and support.

Chapter 1 Introduction

1.1 Multiferroic and Magnetoelectric Materials

"Multiferroics" stands for materials that possess two or more primary ferroic properties in the same phase: including ferroelectricity, ferromagnetism, ferroelasticity and ferrotoroidicity [2, 3]. Since the term multiferroics was coined by Schmid in 1994 [2], the concept has attracted substantial interest not only because of the unique physical properties but also because its potential technological applications. In multiferroic materials, the coexistence of multiple ferroic orders leads to mutual coupling, either direct or indirect, as illustrated in Figure 1.1a [4]. For example, a magnetic field **H** can control the electric polarization P, and an electric field E can control the magnetization **M** in magnetoelectric multiferroics. Use of multifunctional multiferroic materials as a single device component thus becomes increasingly appealing as the community moves toward miniaturizing devices for information storage, including memory [5], logic devices [6, 7] and nanoscale sensors [8]/actuators [9]. In particular, the coupling between ferromagnetic and ferroelectric order is capable of producing magnetoelectric effect as well as converse magnetoelectric effect, which is at the basis of energy-efficient non-volatile memory and microfluidic devices [10].

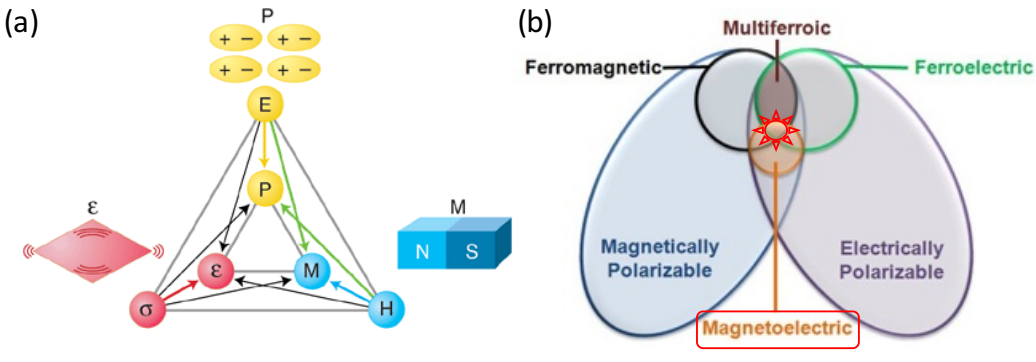

Figure 1.1. (a) Additional interactions due to coexistence of at least two ferroic orders in multiferroics. (Ref.[1], © AAAS.) (b) Venn diagram illustrating the relationship between

multiferroic and magnetoelectric materials. (Ref.[2], © Macmilan Publishers Ltd.: Nature 2006)

1.2 Composite Multiferroics Heterostructures and Electric-field control of Magnetization

Multiferroics that exhibit both ferromagnetic (FM) and ferroelectric (FE) properties have attracted substantial interest owing to the strong magnetoelectric (ME) coupling behavior between these two ferroic orders.

Single-phase multiferroics have relatively low magnetoelectric coupling coefficients due to the reciprocity relations that limit magnetoelectric susceptibilities [10, 11]. Compared to single-phase multiferroics, composite multiferroic heterostructures are particularly important for their larger ME coupling effect, where coupling has been demonstrated via several methods, including elastic strain, exchange bias effect, and charge carrier density - all controllable by electric field [6, 12]. Among these, the use of electrical field to actuate strain-coupled multiferroic heterostructures has been widely demonstrated in the past few years as an energy-efficient pathway for controlling magnetization in the FM layer [13-15]. Figure 1.2 demonstrates an example of a composite multiferroic structure with FM Ni microstructures on FE [Pb(Mg1/3Nb2/3)O3]0.66–[PbTiO3]0.34 (PMN-PT) substrate, controlled by an applied electric field which generates in-plane strain. The anisotropic strain subsequently drives domain wall motion in Ni rings.

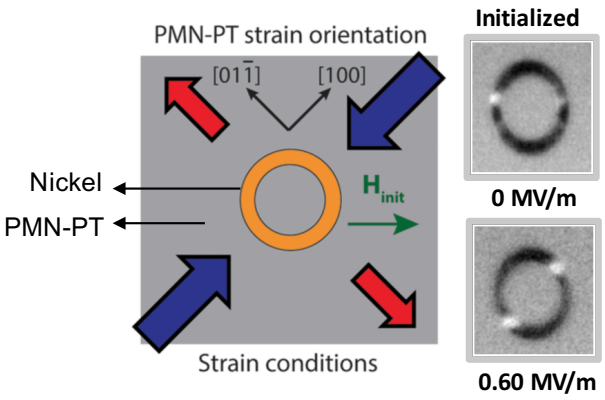

Figure 1.2. Strain-mediated multiferroic heterostructures with magnetic domain rotation in Ni rings. (Ref. [3], © ACS Nano)

In previous works, the behavior of these complex coupled systems was predicted and interpreted mostly by using a unidirectional model, which primarily describes the influence of strain on the system's magnetic ground state by the inverse magnetostrictive effect. This works well for describing the behavior of systems with small magnetostrictive coefficients. However, growing interest in using highly magnetostrictive materials in composite multiferroic systems prompts the need for a more accurate representation of the systems behavior where the influence of the magnetic state on the strain configuration is crucial. This work represents the first comparison of unidirectional and bidirectional modeling of a multiferroic hetero-structure, indicating the need and importance of using models that accounts for bidirectional magneto-elastic coupling. This work not only points out the shortcomings of commonly used unidirectional models, but also stresses the need to consider bidirectional coupling, especially for the highly magnetostrictive materials that are increasingly used in experimental research. The comparison of modeling results for both highly and weakly magnetostrictive materials disproves the prevalent thought that the use of higher magnetostrictive material can always simply result in proportional larger changes in magnetization. In fact, we found that back coupling of magnetization to strain can actually inhibit formation and rotation of magnetic states in some cases, highlighting the need to undo the assumption that unidirectional modeling always captures the necessary physics in multiferroics.

Moreover, enhancing the magnetoelectric coupling in a strain-mediated multiferroic composite structure plays a vital role in controlling magnetism by electric fields. An enhancement of magnetoelastic coupling between ferroelectric single crystal (011)-cut $[Pb(Mg_{1/3}Nb_{2/3})O_3]_{(1-x)}$-$[PbTiO_3]_x$ (PMN-PT, $x \approx 0.30$) and ferromagnetic polycrystalline Ni

thin film through an interposed benzocyclobutene polymer thin film is reported. A nearly twofold increase in sensitivity of remanent magnetization in the Ni thin film to an applied electric field is observed. This observation suggests a viable method of improving the magnetoelectric response in these composite multiferroic systems.

1.3 General Topics and Brief Content of the Thesis

This thesis is composed of the following five chapters: Chapter 1 introduces the concept and fundamental physical phenomenon of multiferroic materials with a focus on strain-mediated composite multiferroics and magetoelectric couling effects. Chapter 2 focuses on magnetostrictive microstructures and two modeling approaches to highlight the need to include bi-directional coupling model to describe the magnetization behavior in highly magnetostrictive materials. Chapter 3 examines the strain distribution with a resolution on par with the microstructure dimension to explains the non-uniform response of microstructure to electrically-induced strain. Chapter 4 investigates the enhanced magnetoelectric coupling as a result of interposing a polymer layer between ferromagnetic and ferroelectric layers. Chapter 5 is the summary and outlook.

Chapter 2 Magnetostrictive micro structures Nickel and Terfenol-D

2.1 Introduction

Controlled magnetization motion, including domain-wall (DW) and domain state rotation, in miniaturized multiferroic heterostructures creates the possibility of new types of devices in a range of applications, including memory [4], logic devices [5, 6] and nanoscale sensors [7]/actuators [8]. Previous micro/nanoscale DW-based devices used either external magnetic field or current-based methods to manipulate DWs [9]. However, the external magnetic field approach fails to realize localized magnetic state switching, and current-based approach suffers from power consumption and thermal management issues due to Joule heating [10]. Alternative approaches to control DW and magnetization motion at micro/nanoscale are thus required to address these issues.

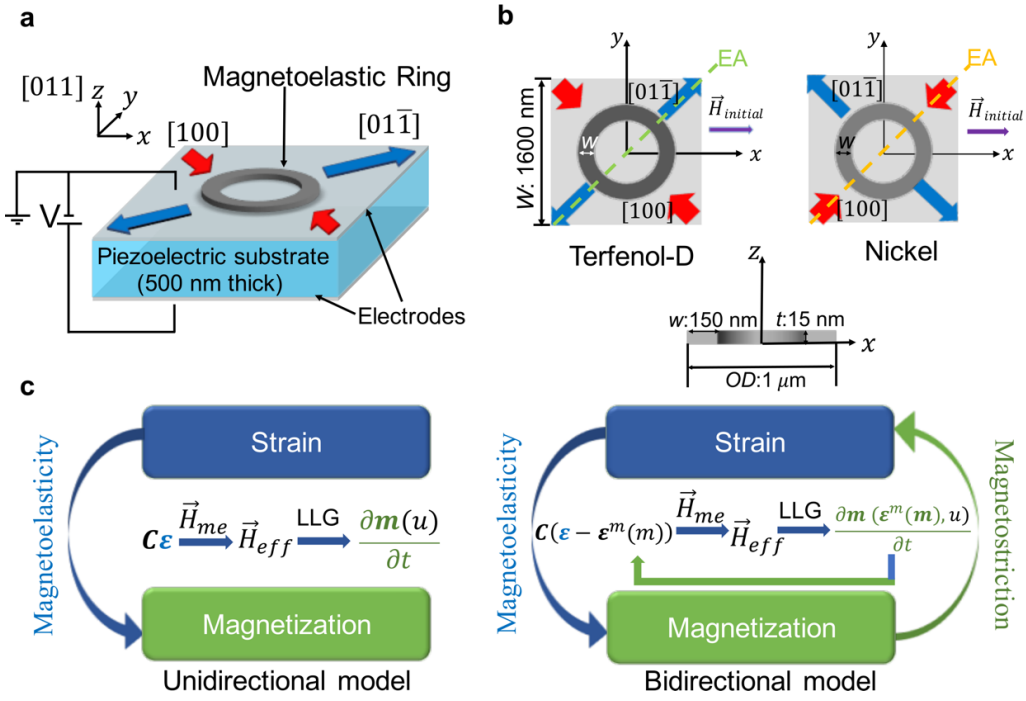

Figure 2.1. Schematic illustrations of (a) setup for the electrical-field controlled strain-mediated rotation of magnetic domain states in a ferromagnetic ring on top of piezoelectric substrate PMN-PT with a 500 μm thickness. (b) Top view and cross section view of the magnetoelastic rings (Terfenol-D and Ni) with outer diameter (*OD*) of 1 μm, width (*w*) of

150 nm and thickness (t) of 15 nm. Illustration of the initialization field $\vec{H}_{initial}$ with respect to the crystal orientations in PMN-PT for both Terfenol-D and Ni rings, and the tensile and compressive response along corresponding directions. Substrate width is 1600 nm. E.A. indicates the strain-induced magnetic easy-axis due to magneto-elastic coupling. (c) Description of the two simulation approaches: the unidirectional model only tracks inverse magnetostrictive effect; while the bidirectional model considers both the magnetostrictive and inverse magnetostrictive effects.

The use of electric fields to control magnetization through multiferroic coupling subsequently emerged as an alternative due to the favorable scaling of electric fields as compared to currents [3, 11-17]. Strain-coupled multiferroic heterostructures, which consist of a non-magnetic\ferromagnetic bilayer, have been investigated as an alternative pathway to achieve energy efficient magnetization control at room temperature [2, 5, 8, 18]. In particular, strain-coupled multiferroics have a ferromagnetic (FM) layer and ferroelectric/piezoelectric substrate (strain-mediated approach) where the strain in the piezoelectric layer alters the magnetic anisotropy in the FM layer (Figure 2.1a and 2.1b) [19].

Manipulation of magnetization via the strain-based approach has already been demonstrated experimentally in Ni [3, 20, 21], CoFeB [22], FeGa [23] , Fe and CoFe [11] on piezoelectric substrates. Increasing interest in highly magnetoelastic materials, such as Terfenol-D ($Tb_xDy_{1-x}Fe_2$, x = 0.3) with magnetostriction saturation $\lambda_s = 1200 \times 10^{-6}$ [24], creates the need for thorough understanding of the magnetization behavior inside these materials owing to their potential for enhanced strain-mediated DW rotation [25-28]. Much of the prior work that uses unidirectional (UD) model has produced comparable results to the experimental observations, even though strain induced by the change in magnetization is generally ignored [29-32]. A UD model only tracks magnetoelastic coupling in one direction, i.e. a static electric-field produces a strain which changes the magnetic anisotropy but does not feedback to the initial equilibrium strain state. However, these results usually focus on

weakly magnetoelastic materials, including pure transition metal ferromagnets such as Ni ($\lambda_s = -33 \times 10^{-6}$) [31]. For materials such as Terfenol-D, with a much larger saturation magnetostriction, previous UD models may no longer be adequate for describing the system, and thus require a more rigorous approach. In the aforementioned multiferroic heterostructures (Figure 1a), not only will the strain in the piezoelectric substrate influence the magnetic anisotropy in the magnetic film owing to the inverse magnetostrictive effect (Villari effect) [33], but also the change in magnetization in the film will in turn feedback to the piezoelectric material via the magnetostrictive effect. A bidirectional (BD) model can fully account for such an interaction. To understand the differences between the two approaches, we compare the simulated magnetic domain and DW rotations in both Ni and Terfenol-D disks and rings for different voltage-induced strains.

In this chapter, we first investigate the initialized DW states in magnetic structures at equilibrium using both the UD and BD modeling approaches. We consider two common elements in multiferroics, rings and disks [34, 35], due to their radial symmetry and smooth sidewalls. We then apply strain to the structures and study the strain-induced domain motion predicted by the two approaches, with the resulting magnetic states compared and contrasted. The simulation results show that for weakly magnetoelastic materials (e.g. Ni, Co and CoFeB)[3, 32, 34],[36] with applied strain, the influence of magnetostriction is likely negligible, and UD models are sufficient. However, the transition to highly magnetoelastic materials (e.g. Terfenol-D) requires a more accurate accounting of the coupling, and BD models should therefore be considered. We also report classifications of initialized magnetization configurations in Terfenol-D rings with different dimensions and present a phase diagram of equilibrium magnetic domain states (see Appendix A. Initial Magnetization Classification), which lays the groundwork for properly designing Terfenol-D ring systems. The focus of this study is the behavior of the nucleated magnetic DWs (see Appendix A) or

magnetic domains in response to such strain. This is due to the fact that the localized magnetic stray field from the DWs and domains can be utilized in actual technological applications, such as nanoparticle manipulation in microfluidic environments [37, 38].

2.2 Modeling setup

The schematic of the modeling setup for electric-field controlled, strain-mediated DW rotation in a ring is illustrated in Figure 2.1a. A piezoelectric substrate, $[Pb(Mg_{1/3}Nb_{2/3})O_3]_{0.66}$–$[PbTiO_3]_{0.34}$ (PMN–PT), with a size of 1600 nm × 1600 nm × 500 nm (thickness) is placed underneath a magnetoelastic ring or disk. The bottom surface of the PMN-PT is clamped with no displacement, and the four sides of the PMN-PT substrate are also clamped (see Appendix B) [39]. Simulations of varying substrate sizes verified that the chosen substrate is sufficiently large to accurately model the strain in the magnetic structures. The ring dimension (Figure 2.1b) is chosen as 1000 nm outer diameter (*OD)* with 150 nm width (*w*) and 15 nm thickness (*t*) so that the initialized stable state before strain application is an onion state with transverse DWs [20], with a large total energy density (see Appendix A for a list of geometry-dependent initial states). The disk dimension is chosen with 1000 nm in diameter and 15 nm in thickness. The choice of the 15 nm thickness for the magnetic structures ensures that the strain is effectively transferred across the entire magnetic layer thickness [40].

The magnetic states of the ring and disk are initially set in equilibrium states, representing the remanent state after removal of an external magnetic field that initially saturated the state in the $+x$ direction. Once the field is removed, the magnetization falls into a magnetically-relaxed state due to minimization of the total energy [20, 35], including demagnetization energy (shape anisotropy energy) and exchange energy. For a ring, this step generates the nucleation of two DWs in diametrically opposite position.

After the initialization process, an electric field is applied through the thickness of the PMN-PT [011] substrate, which is in a pre-poled ferroelectric state, with polarization pointing up (or down). In such strain-mediated multiferroic approach, a voltage applied to the PMN-PT substrate induces anisotropic strain in the magnetoelastic structures. This results in a mechanical compressive strain along the [100] direction, and tensile strain along the $[01\bar{1}]$ direction of the piezoelectric substrate (see Appendix B). The electrically-induced strain is then transferred into the ring and the disk. Magnetostrictive materials usually exhibit complicated domain structures to minimize total free energy, which is determined by the competition among exchange energy, demagnetization energy and magneto-elastic energy [39, 41]. With the presence of applied strain, reorientation of the domain states take place because of such competition.

In a Terfenol-D ring, as shown in Figure 2.1b, the transferred mechanical strain tends to orient the DWstoward the *tensile* strain axis direction $[01\bar{1}]$ in PMN-PT (45^o from the +*x* axis) due to a *positive* magnetostriction effect [42, 43]. On the other hand, for a Ni ring on PMN-PT (see Figure 1b), DWs tend to rotate toward the *compressive* strain direction [100] due to the *negative* saturation magnetostriction of Ni. Therefore, different from the Terfenol-D ring system setup, for the piezoelectric substrate underneath Ni ring, compressive strain is induced along 45^o from the +*x* axis (also [100] direction), and tensile strain along -45^o to the +*x* axis (also $[01\bar{1}]$ direction) to produce DW rotation in the same counter clockwise direction as that in Terfenol-D rings to make clear comparisons (see Figure 2.1b for more details).

In actual ring devices, the strain is not uniformly transferred from the piezoelectric to the ferromagnetic layer, resulting in a non-uniform magneto-elastic energy density through the ring width and thickness. Non-uniformity of the strain arises from different mechanisms, such as shear lag effects of the strain and anisotropy in the piezoelectric substrate [39]. Due to the

non-uniform strain distribution in the system, mapping of the time-dependent inhomogeneous strain states is required in the modeling.

2.3 Computational Details

We simulated the strain-induced magnetization change using both the BD and UD models. For both models, the micromagnetic and elastodynamic partial differential equations (PDEs) are implemented in the weak form and are solved using the finite element method. However, the two models differ because the BD model, differently from the UD model, incorporates stress induced via magnetostriction, iterating between stress-induced changes in magnetization, and magnetization-induced stress until a solution is found.

From the magnetic point of view, the time evolution of the normalized magnetization $\boldsymbol{m}$ ($|\boldsymbol{m}| = 1$) is determined by the micromagnetic relation that satisfies the Landau-Lifshitz-Gilbert equation (LLG). LLG describes the precessional dynamics and relaxation of the magnetization vector: $\frac{\partial \boldsymbol{m}}{\partial t} = -\mu_0\gamma(\boldsymbol{m}\times\boldsymbol{H_{eff}}) + \alpha\left(\boldsymbol{m}\times\frac{\partial \boldsymbol{m}}{\partial t}\right)$, where μ_0 is the vacuum permeability, γ is the gyromagnetic ratio and α is the Gilbert damping constant. For Ni, the experimentally measured α is 0.038 [44, 45], and for Terfenol-D it is 0.06±0.02 [46]. In our simulations, the major goal is to compare the final static state after strain is applied, so α is set to 0.5 to achieve equilibrium in a reasonable calculation time. The damping factor is expected to affect the magnetization dynamics, including the speed with which the DW/domain will move and the time that will take for the magnetization to reach its stable state. However, it is not expected to affect the final state itself, which is determined by the minimization of total free energy [39]. In our study, we induce a uniaxial magnetic anisotropy which will induce the magnetization to realign. This reorientation is expected to be fully deterministic if a magnetization rotation of an angle smaller than 90^o is induced, which is the case in this study. Accordingly, we do not expect the larger damping factor to influence at all

the final magnetic state induced by the applied strain via magneto-elastic coupling. The effective magnetic field $\boldsymbol{H_{eff}}$ is defined as $\boldsymbol{H_{eff}} = -\frac{1}{\mu_0 \boldsymbol{M_s}} \frac{\partial E_{tot}}{\partial m}$, where E_{tot} is the total energy density and $\boldsymbol{M_s}$ is the saturation magnetization.[47] In our model, $\boldsymbol{H_{eff}}$ is expressed as the summation of the external field ($\boldsymbol{H_{ext}}$), exchange field ($\boldsymbol{H_{ex}}$), demagnetization field ($\boldsymbol{H_d}$) and magnetoelastic field ($\boldsymbol{H_{me}}$) [39, 48]. Among these fields, the magnetoelastic field $\boldsymbol{H_{me}}(\boldsymbol{m}, \boldsymbol{\varepsilon^{tot}})$ depends on both $\boldsymbol{m}$ and the total strain $\boldsymbol{\varepsilon^{tot}}$. Solving these equations using the finite element method allows us to determine the final magnetization of the magnetic structure.

From the mechanical point of view, the displacement field $\boldsymbol{u}$ obeys the elastodynamic equation $\rho \frac{\partial^2 \boldsymbol{u}}{\partial t^2} = \nabla \cdot \boldsymbol{\sigma}$, where ρ and $\boldsymbol{\sigma}$ denote the volumetric density and the stress tensor, respectively.[6, 39] Thus, the constitutive relation between the stress tensor $\boldsymbol{\sigma}$ and the elastic strain tensor $\boldsymbol{\varepsilon^{el}}$ can be expressed as $\boldsymbol{\sigma} = \boldsymbol{C}\boldsymbol{\varepsilon^{el}}$, where $\boldsymbol{C}$ is the elastic stiffness tensor. In magnetoelastic materials that are also cubic crystals, the magnetoelastic strain tensor $\boldsymbol{\varepsilon^m}$ is induced by $\boldsymbol{m}$: $\varepsilon_{ii}^m = \frac{3}{2}\lambda_{100}(m_i^2 - \frac{1}{3})$ and $\varepsilon_{ij}^m = \frac{3}{2}\lambda_{111} m_i m_j (i \neq j)$, where λ_{100} and λ_{111} represent the magnetostriction constants in <100> and <111> directions, respectively. $\boldsymbol{\varepsilon^m}$ also contributes to $\boldsymbol{\varepsilon^{tot}}$, namely $\boldsymbol{\varepsilon^{tot}} = \boldsymbol{\varepsilon^{el}} + \boldsymbol{\varepsilon^m}$.

The major difference between the BD and UD models originates from the way in which the strain is being treated. In the conventional UD model, elastic stain $\boldsymbol{\varepsilon^{el}}$ is assumed to be the only strain contributing to the magnetoelastic effects, and is thus equivalent to the total strain $\boldsymbol{\varepsilon^{tot}}$ (see Figure 2.1c, left). Therefore, elastodynamics and micromagnetics are not fully coupled, as the magnetization is calculated in the following steps: a) $\boldsymbol{\varepsilon^{tot}}$, which equates to $\boldsymbol{\varepsilon^{el}}$ in UD models, is calculated first by solving the elastodynamic equation, b) $\boldsymbol{\varepsilon^{tot}}$ is incorporated into the LLG equation via $\boldsymbol{H_{me}}$ to calculate $\boldsymbol{m}$ in the magnetoelastic structure.

On the other hand, in the BD model, the total strain $\boldsymbol{\varepsilon^{tot}}$ takes into account contributions from both the linear elastic strain and the magnetic strain. It solves the intrinsically coupled PDEs simultaneously: a) $\boldsymbol{\varepsilon^{tot}}$, which equates to $\boldsymbol{\varepsilon^{el}}$+$\boldsymbol{\varepsilon}^m$, is calculated from the elastodynamic equation, b) $\boldsymbol{\varepsilon^{tot}}$ is incorporated into the LLG equation via $\boldsymbol{H}_{me}$ to calculate $\boldsymbol{m}$ as well as $\boldsymbol{\varepsilon}^m$, and c) the generated magnetic state is fed back into the elastodynamic equation and the above steps are repeated until reaching convergence. As shown in Figure 1c (right), magnetization change causes change in strain by affecting $\boldsymbol{\varepsilon^m(m)}$, and hence $\boldsymbol{H}_{me}$. Consequently, the time-dependent distribution of magnetization vectors $\boldsymbol{m}$ $(\boldsymbol{\varepsilon}^m(\boldsymbol{m}), u, t)$ in the magnetoelastic structure, which responds to both displacement field $\boldsymbol{u}$ and recurring changes in effective strain imposed by $\boldsymbol{\varepsilon}^m(\boldsymbol{m})$, continue to modify $\boldsymbol{\varepsilon^m(m)}$ and thus $\boldsymbol{H}_{me}$ (as illustrated by the green arrow in Figure 2.1c, right). This bidirectional model captures the bilateral communication/interaction between strain and magnetization via both Villari effect and magnetostrictive effect (see Figure 2.1c).

By comparison, the BD model more fully captures the physics in the coupled magnetoelastic system. The decoupling in the UD model assumes that the magnetostriction coefficient is very small. Hence, the elastic strain is approximately equal to the total strain ($\boldsymbol{\varepsilon}^{tot} \approx \boldsymbol{\varepsilon}^{el}$). However, when dealing with materials with high magnetostriction constants, the BD and UD models lead to drastically different results.

2.4 Results and Discussions

A finite element simulation using micromagnetic/elastodynamic model was developed using COMSOL [42]. The simulation reproduces the initialized "onion" domain state in the Terfenol-D ring as shown in Figure 2.2a from unidirectional simulations (left), and from bidirectional simulations (right). Similarly, the initialized magnetization states in Ni rings with the same dimensions can be seen in Figure 2.3a.

For a Terfenol-D ring, even though both modeling methods yield an "onion state", the initial states formed in the simulations based on the UD and BD models are different. The reason for such difference lies in the fact that the FM layer is mechanically-coupled strongly to the FE substrate. For BD modeling, the saturated state initiated to +*x* direction gives more hindrance to the subsequent relaxation due to the strong clamping, thus showing "ripple-like" magnetization distribution when stable. The magnetization direction oscillates periodically along the circumferential direction of the top and bottom side of the ring surface for the bidirectional model. However, no oscillations in the magnetic state are observed from the unidirectional model (see Figure 2.2a for comparison). On the contrary, in the less magnetostrictive Ni ring, the two modeling approaches predict almost identical initial states: the magnetization direction exhibits a smoother distribution along the circumferential direction of the ring (see Figure 2.3a).

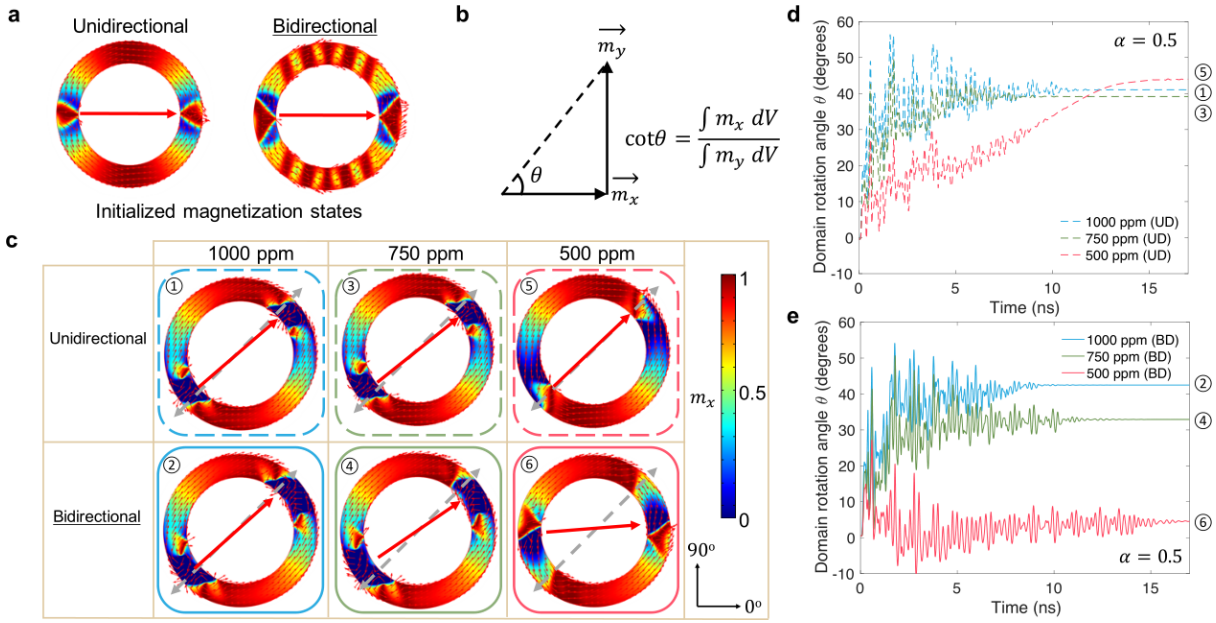

Figure 2.2. (a) Results of finite element simulations for the initialized magnetization state in Terfenol-D ring (*OD* of 1 μm, *w* of 150 nm, *t* of 15 nm) at equilibrium, using unidirectional model (left panel) and bidirectional model (right panel). (b) Domain rotation angle is defined as the ratio between the volume average of magnetization along +*x* axis and that along +*y* axis. (c) Magnetization distribution and domain rotation state resulting from

both models under applied strain of 1000 ppm, 750 ppm and 500 ppm. Solid arrow (in red) defines the final position (after rotation) of the two DWs, while the dashed arrow (in gray) indicates the orientation of the tensile strain. The color gradient bar represents magnetization component along +x axis. ①- ⑥ are the surface view of stabilized magnetization states after strain is applied. (d)-(e) DW rotation angle as a function of time when tensile strain is generated along the direction 45^o to the +x axis, for UD and BD models, respectively. Simulation time scale is based on damping factor α = 0.5 (time scales are for relative comparison between simulations). The numbers adjacent to the domain rotation angles at equilibrium correspond to the domain state configurations shown in (c).

When an electric field is applied to the piezoelectric material, a strain is generated and transmitted to the magnetoelastic material. This strain alters the magnetoelastic energy, causing the onion state to re-orient toward its new energy minimum configuration and driving the DWs towards the direction of the principal strain axes (i.e., compressive directions for Ni and tensile direction for Terfenol-D, respectively). Time-dependent DW rotations are tracked and compared for both UD and BD models. In the case of Terfenol-D rings, we observe in the BD models that feedback from magnetostriction prevents rotation of the DW at lower strain values. The domain rotation angle, θ, is estimated by calculating the ratio of volume averages of the x-direction and y-direction component of magnetization, as reported in Figure 2.2b. As shown in Figure 2.2c, the unidirectional model yields full rotation for strain of 1000 ppm (c-1), 750 ppm (c-3), and 500 ppm (c-5). However, the bidirectional model produces a more complex result, where applying a 1000 ppm strain fully rotates the "onion state" to the magnetic easy axis (θ =45^o, c-2); a 750 ppm strain only partially rotates the domain state to 33^o (c-4) and a 500 ppm strain results in minimal rotation of the domain state of 5^o (c-6). This is due to the significant influence of the magnetostriction feedback from Terfenol-D rings to the piezoelectric substrate. The time-dependent domain rotation as predicted by both models is shown in Figure 2.2d and Figure 2.2e.

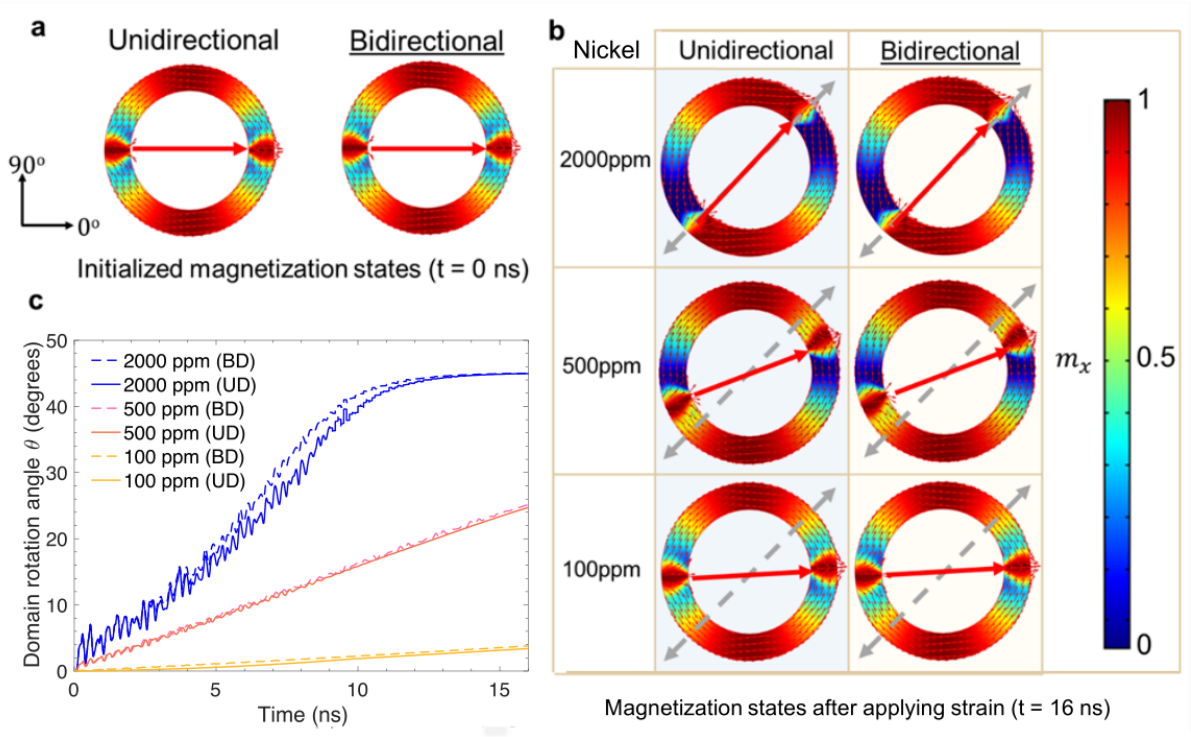

Figure 2.3. (a) Results of finite element simulations of initialized magnetization state of a 15 nm thick, 150 nm wide, 1 μm outer diameter Ni ring at equilibrium. Left panel, result from unidirectional model. Right panel, result from bidirectional model. (b) DW rotation state in Ni rings at 16 ns after strain application predicted by two models when subjected to 2000 ppm, 500 ppm and 100 ppm strains. (c) DW rotation angle as a function of time as the strain is applied to the piezoelectric substrate at 45° to the $+x$ axis (damping factor $\alpha = 0.5$ used in simulation), with results from both UD and BD models.

In contrast, for the Ni ring, both modeling approaches give rise to similar DW rotation. due to the small magnetostriction feedback present in Nickel, as shown in Figure 2.3b. For Ni, it appears that regardless of the strain magnitude, the DWs fully rotate as long as enough time is given. One explanation is that the low magnetostriction coefficient generates a negligible magnetostrictive effect, which would reduce the initially applied strain.

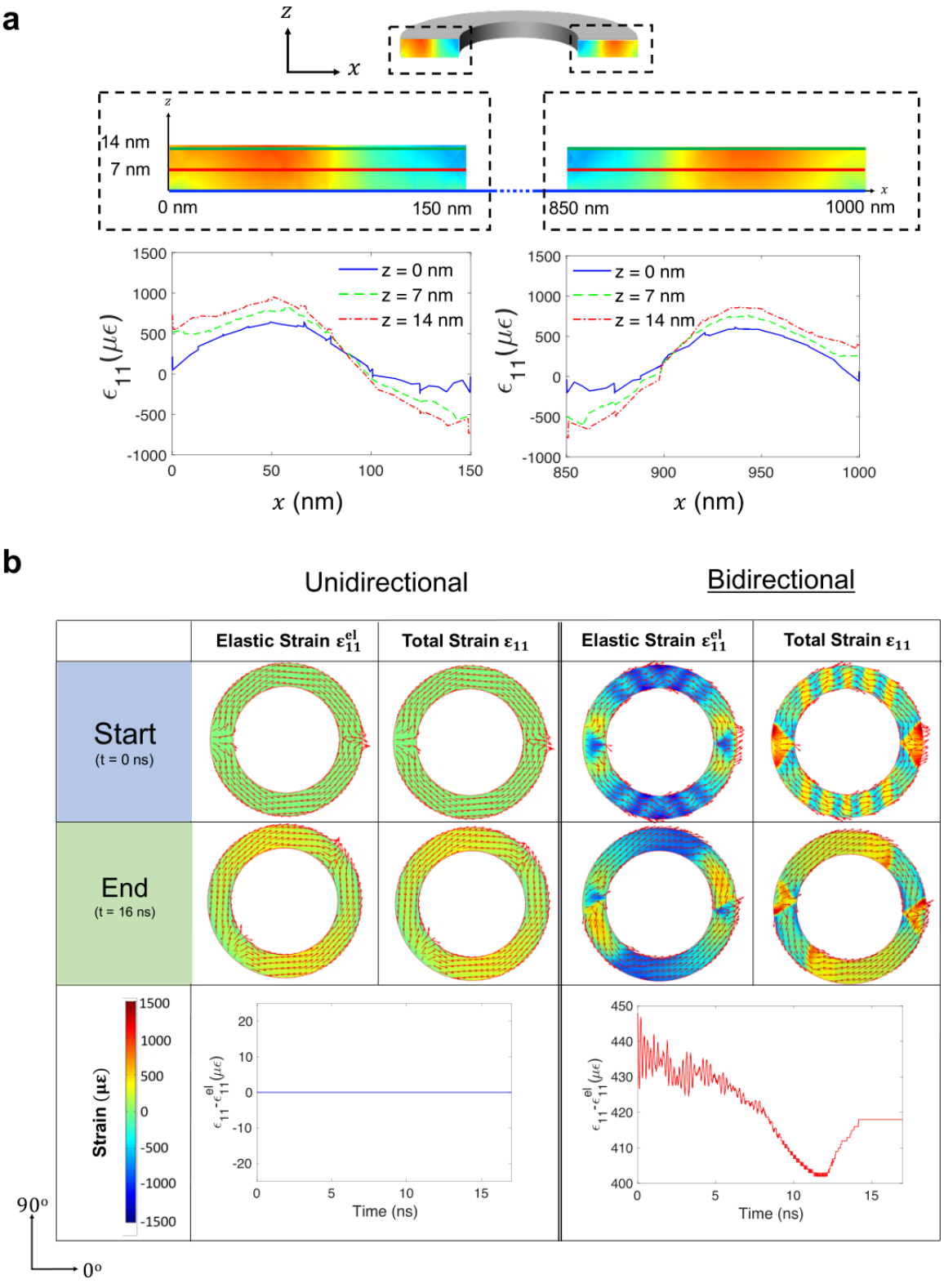

Figure 2.4. (a) Non-uniform strain distribution across the *xz*-plane in the Terfenol-D ring at steady state after applying a strain of 500 ppm using the bidirectional model (top panel) and corresponding strain value as a function of position *x* at three different heights *z* (bottom panel). (b) Top view of strain distributions at equilibriums in the ring before and after

applying strain (top panel) and difference between total strain and elastic strain as a function of time predicted by two modeling approaches (bottom panel).

To further investigate the difference between these two modeling approaches, we study the size effects in the present microrings. Indeed, we simulate the strain distributions in the ring before and after a strain of 500 ppm is applied to the substrate and transferred to the ring. The non-uniform strain profile in the ring calculated by the bidirectional model is explicitly shown in Figure 2.4a. In addition, total strain distributions at different thickness (z values) as a function of x are plotted to demonstrate the variation of the strain through the thickness of the micro-ring. The difference between total and elastic strain (Figure 2.4b), which is zero for UD models and non-zero for BD models, confirms the non-negligible effect of magnetostriction in Terfenol-D. Comparison between the patterns of surface strain mapping plots in the bidirectional model (Figure 2.4b) and their corresponding magnetization states (Figure 2.2a and Figure 2.2c) also indicates the strong coupling between strain and magnetization.

In order to demonstrate that the importance of the bidirectional modeling approach is not limited only to ring structures, we applied the model to a faster response system, nanometer scale disks, to confirm that the advantage of such model will also be applicable to a wide range of geometries. For a Terfenol-D disk of 200 nm in diameter and 15 nm thick, the equilibrium states at initialization are found to be different. The UD model predicts a single domain state pointing along the initializing magnetic field (+x axis, 0^o), while the BD model shows an "S" shape domain with average magnetization pointing along 22^o (Figure 2.5a). The equilibrium magnetic state for Terfenol-D is captured by the BD model, making evident the role of magnetization-induced magnetoelastic strain, ε^m. After applying strain with the BD model, the level of domain rotation in Terfernol-D disk is determined by the magnitude of the applied strain. On the contrary, for a Ni disk of the same dimension, both UD and BD model

coincides well with each other, with both yielding a single domain pointing along 0^o. When driven by applied strain, the obtained domain state (average magnetization) rotations in the UD and the BD models are equivalent. (Figure 2.6)

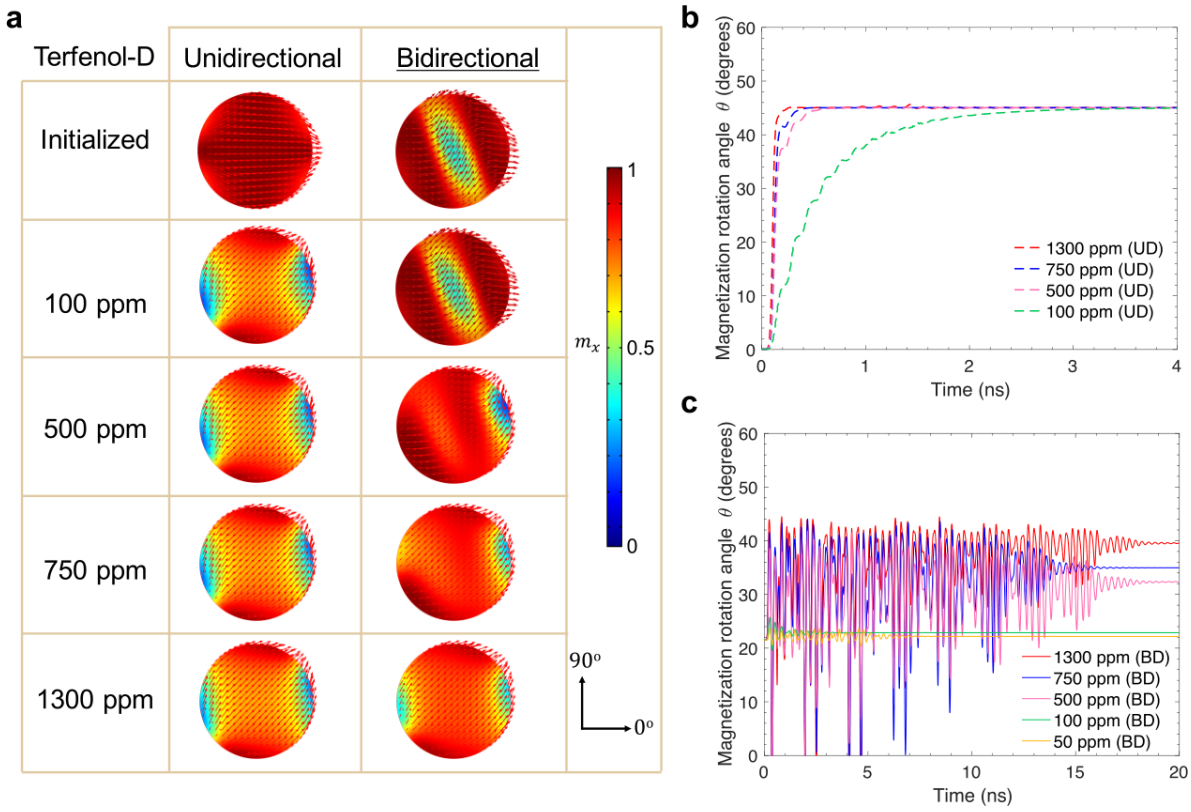

Figure 2.5. (a) Results of finite element simulations of initialized magnetization state of a 15 nm thick, 200 nm diameter Terfenol-D ring at initialization state and at equilibrium after application of strain, predicted by UD and BD models when subjected to 100 ppm, 500 ppm, 750 ppm and 1300 ppm strain. (b) and (c) Domain state rotation angle as a function of time (damping factor $\alpha = 0.5$), obtained by the UD and the BD models, respectively.

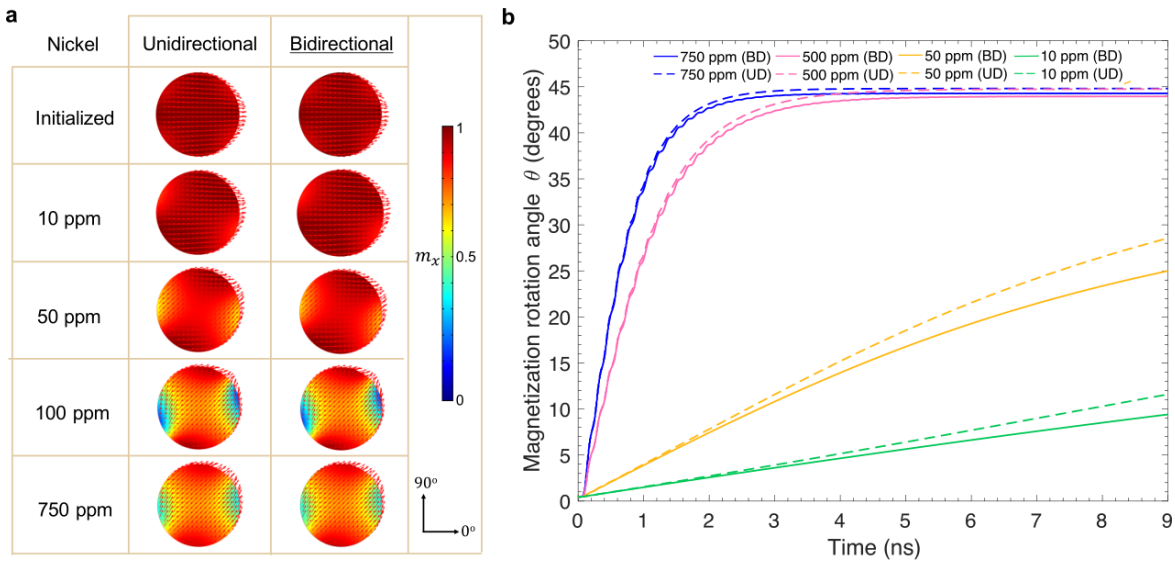

Figure 2.6. (a) Results of finite element simulations of initialized magnetization state of a 15 nm thick, 200 nm diameter Ni ring at initialization state and equilibrium after strain application, predicted by two models when subjected to 10 ppm, 50 ppm, 100 ppm, and 750 ppm strain. b) Domain state rotation angle as a function of time as the strain is applied to the piezoelectric substrate at 45° to the $+x$ axis (damping factor $\alpha = 0.5$), with results from both UD and BD models.

The use of BD modeling is most important in cases with highly magnetostrictive materials with low to moderate strain. For weakly magnetoelastic materials, UD and BD models provide similar predictions for strains in the typical range of interest. Whereas for strongly magnetoelastic materials, UD models over predict the rotation of magnetic domains/DWs compared to the more comprehensive BD models. As the strain approaches magnetization saturation $\lambda \approx \lambda_s$, the predictions of UD and BD models converge. The applied strain is typically smaller than the saturation magnetization ($\lambda_s = 1200\times 10^{-6}$ for Terfenol-D), which implies that BD models should generally be used for highly magnetostricive materials. Furthermore, even though the modeling results do not reflect the actual timescale due to selection of α, comparison of time-dependent strain rotation plots at different strain levels indicate that the speed of the movement of domains is strain-dependent. With larger applied strain, the domain moves more rapidly.

Finally, it should be noted that the comprehensive bidirectional computational approach here discussed fully captures the magnetic behavior of strain-based multiferroic heterostructures. The unidirectional approach may be helpful for simplifying computation, but does not accurately reflect the behavior of systems in cases where the feedback from magnetization to the strain is comparable to the inverse magnetostrictive effect**.** This work explains the nuance in coupling between strain and magnetism for the two modeling approaches. The most relevant result is that the two modeling approaches arrive at drastically different predictions in both the equilibrium state and the degree of strain-induced domain rotation. Instead of only leading to a binary result of either full rotation or no rotation as in the case of a unidirectional model, the bidirectional model can produce partial rotation for an intermediate range of applied strains. For the Terfenol-D ring in the bidirectional scenario, strain of 750 ppm does not fully rotate the onion states to 45^{o}, and strain of 500 ppm only minimally rotates the magnetic DWs. The final angle of rotation at equilibrium falls between 0 and 45^{o} depending on the competition between inverse magnetostrictive effect and magnetostrictive effect. Similarly, for the Terfenol-D disk in the bidirectional cases, strains of 750 ppm and below do not fully rotate the domain state due to the additional strain term $\boldsymbol{\varepsilon}^{m}(\boldsymbol{m})$. For 1000 ppm strain, UD result is on a par with that of BD because the strain value is close to Terfenol-D's magnetostriction coefficient. Therefore, simply by using highly magnetostrictive materials it does not necessarily lead to an enhanced control of magnetism by strain as compared to weakly magnetostrictive materials.

2.5 Concluding remarks

In summary, we have studied strain-induced domain wall rotation in multiferroic heterostructures using finite element simulations that use both unidirectional and bidirectional coupling approaches. Results from these two types of modeling are compared for strain-

induced magnetic-domain rotation in Ni and Terfenol-D rings and disks. The unidirectional approach, while being commonly used by the micromagnetics modeling community, has limitations when evaluating the behavior of highly magnetoelastic materials (e.g. Terfenol-D). The bidirectional model provides a more accurate description of the coupled systems, implying that the effect of magnetostriction feedback from highly magnetoelastic materials to the piezoelectric substrate is non-negligible. The need for bidirectional modeling is highlighted by the fact that the unidirectional model consistently under-predicts the strain necessary to rotate the magnetization in the Terfenol-D rings. Also, the lack of magnetostriction in unidirectional models leads it to predict different initial equilibrium states (before strain is applied) in some cases. Therefore, utilizing bidirectional modeling is key to the understanding of highly efficient multiferroic devices. In addition to the ring and disk shape geometries and Terfenol-D alloy used for demonstration, the fundamental principles in this work are also pertinent to other highly magnetoelastic materials with various in-plane geometries. In combination with experimental investigations, such a bidirectional model may allow for a better assessment of coupling behaviors within multiferroic devices.

Chapter 3 Strain Distribution in Single Crystal PMN-PT

3.1 Introduction

So far, we have focused on the magnetic properties of the ferromagnetic component in the composite multiferroic heterostructures while assuming that all magnetic microstructures experience a macroscopically uniform strain from the ferroelectric single crystal (e.g., (011)-cut $[Pb(Mg_{1/3}Nb_{2/3})O_3]_{(1-x)}$-$[PbTiO_3]_x$ (PMN-PT, $x \approx 0.30$)). Previous x-ray magnetic circular dichroism-photoemission electron microscopy (XMCD-PEEM) [49] measurement by Buzzi [50] have shown inhomogeneous magnetic behavior of identical Ni nanostructures, and was explained by the presence of multidomain structure in the FE single crystal. Further XMCD-PEEM work by Sohn [35] on Ni microstructure ring arrays also showed dissimilar behaviors of "onion state" from rings located even as close as a few microns apart. In those scenarios, the dimension of the ferromagnetic domain was mainly assumed to be on par with the dimension of the structure size. To the best of our knowledge, there hasn't been a system-level work that quantifies the non-uniform strain as a function of the electric field at these so-called mesocales (100 nm- 10 um), which is in the range of the constitutive grain size, etc. [51] To obtain mechanical properties at such length scale, including strain information, we conducted synchrotron polychromatic scanning x-ray diffraction (micro-diffraction) on beamline 12.3.2 at the advanced light source of the Lawrence Berkeley National Lab.

3.2 Sample Preparation and Characterization

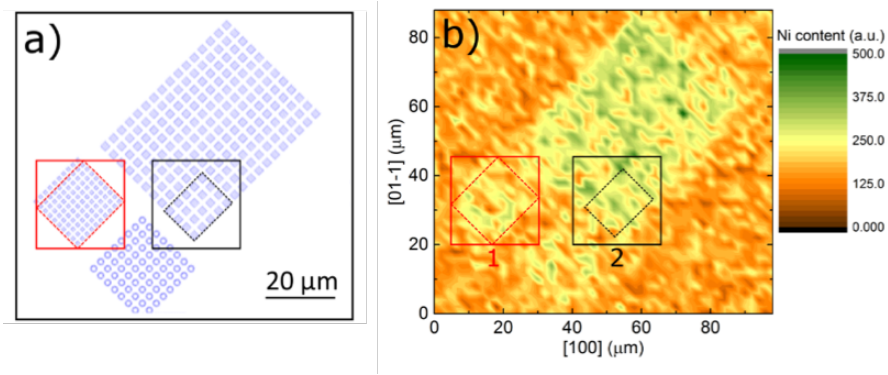

Figure 3.1. (a) Pattern layout of the magnetic square arrays. (b) High-resolution x-ray microfluorescence scan by monochromatic x-ray beam at the Ni L_3 edge of the magnetic microstructures, corresponding to the layout in (a). Areas highlighted by red and black are square arrays of 1 μm and 2 μm, respectively.

We examine both the magnetization and strain distribution of the multiferroic heterostructure composed of Nickel and PMN-PT as electric field is applied to induce strain in the coupled system. The 500 μm thick ferroelectric single crystal [011] PMN-PT substrate is polished on both sides (TRS Technologies, Inc.; State College, PA, USA) and has 50 nm thick Pt electrodes on both sides to form a parallel plate. Before depositing ferromagnetic Ni microstructures on top of it, the substrate is pre-poled in [011] direction. Isolated magnetic square arrays of 1 μm and 2 μm are patterned by electron-beam lithography and are composed of polycrystalline Ni (15 nm)/Ti (5 nm), deposited by e-beam evaporation on the surface of top Pt electrode, followed by lift-off. Figure 3.1a shows the pattern layout of the Ni square arrays and the two arrays in the highlighted inner rectangles are imaged by the XMCD-PEEM. The strain distribution with a resolution of 2 μm of the PMN-PT substrate within the area marked by the two rectangles is examined by X-ray microdiffraction (Figure 3.1b).

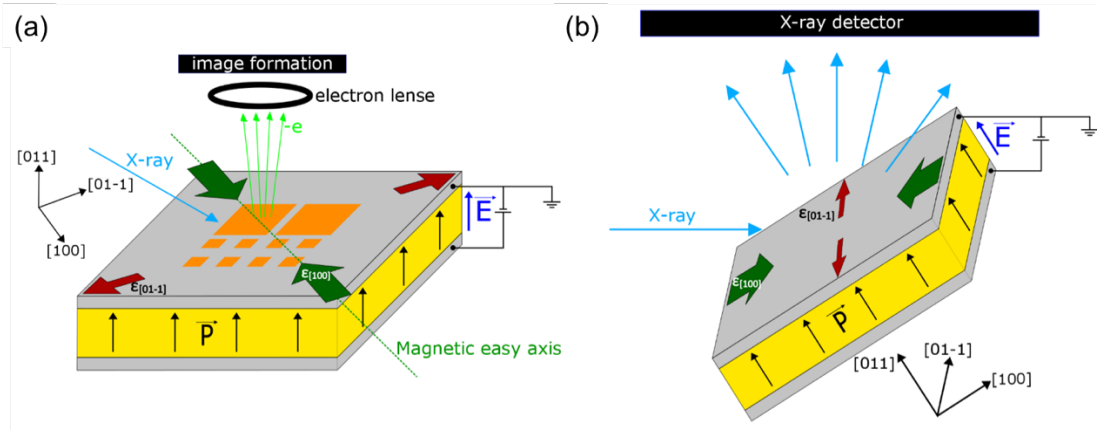

Figure 3.2 (a) Schematic of XMCD-PEEM experiment (not to scale). (b) X-ray microdiffraction experiment setup. The angle between the normal to the sample surface and the incoming x-ray direction is 50°. (Courtesy of Roberto Lo Conte, UC Berkeley)

XMCD-PEEM is used to image the magnetization configurations at different applied electric field, ranging from 0 to 0.66 MV/m. After locating the region of interest (Figure 3.1b) based on fluorescence emission signal of Ni, we focuses on synchrotron polychromatic scanning x-ray technique [51] to raster scan the substrate with a focused white x-ray beam. The step size of the scan is set to be 2 μm (diameter of the beam) which becomes the spatial resolution of the generated strain distribution map. A 2-D Laue diffraction pattern is taken at each step. By comparing with the expected diffraction pattern in unstrained PMN-PT single crystal, the quantitative local strain at the corresponding location can be extracted. Then, a series of analyses and reconstruction of the diffraction pattern yield strain/stress map. The sample is scanned in-plane along both [100] and [01-1] directions of the PMN-PT substrate, which correspond to the compressive and tensile strain directions, respectively. Schematics of both measurements are illustrated in Figure 3.2.

3.3 XMCD-PEEM study of the magnetic squares

XMCD-PEEM characterizes the in-plane magnetization contrast from the square arrays. As the voltage is ramped up with an increment of 30 V from 0 V to 330 V through the 500-

um thickness of the PMN-PT substrate, the electrically-induced magnetic domain formation can be observed across the arrays. Before the imaging, the Ni squares are initialized by a uniform external magnetic field of 0.28 T parallel to the Ni square horizontal edge direction (Figure 3.3). Landau flux-closure state (magnetic vortex state) is observed with subsequent XMCD-PEEM imaging in multiple squares. Not all squares are in the magnetic global minimum energy state (vortex state) partly due to them being in a local minimum single domain state [52]. While the DC electric field is applied across the substrate, in-plane strain is generated in the ferroelectric and subsequently reorients the magnetic moments via Villari effect (inverse magnetostrictive effect) [50]. The reorientation of the magnetic moments in the Ni squares favors [100] direction of the PMN-PT substrate. Therefore, once with adequate strain transferred to the squares, the vortex state evolves to a two-domain state, with magnetization anti-parallel to each other while being both oriented along [100] direction. We note that the electric field required for transforming the initial vortex to two-domain state varies, ranging from 0.18 MV/m to 0.66 MV/m (Figure 3.3). According to the activation statistics for both square arrays, shown in the bottom row of Figure 3.3, the average electric-field required for reorientation in the 2 um squares is lower than that in the 1 um squares. This is because as the magnetic structure increases proportionally in size, the demagnetization energy density decreases and thus smaller strain is required. In addition, comparing the activation electric-field on a row-by-row basis (see black dotted plots of <E> in Figure 3.3 shows a clear spatially-varying factor that contributes to the inhomogeneous response of the magnetic microstructures. Section 3.4 discusses such factor by presenting the inhomogeneous strain-distribution of the substrate underneath these square arrays.

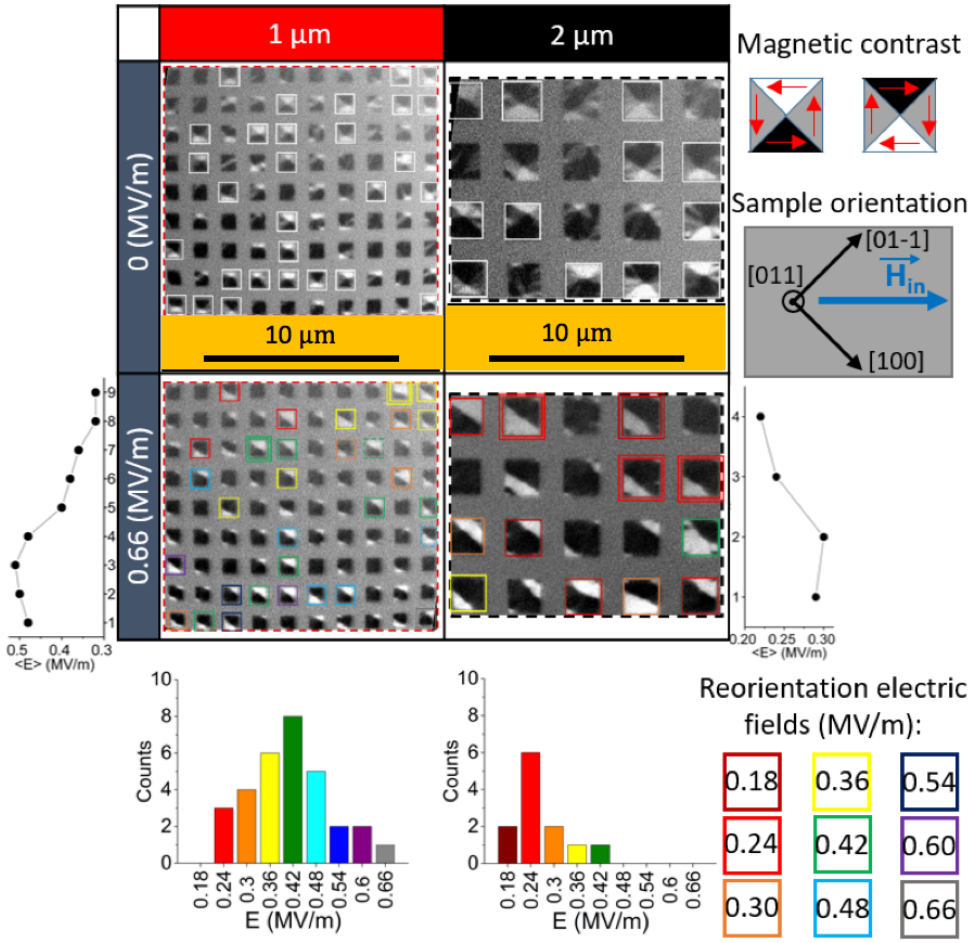

Figure 3.3. XMCD-PEEM images showing the magnetic contrast in 1 μm and 2 μm square arrays before and applying an increasing electric field through the PMN-PT thickness ([011] direction). XMCD-PEEM images taken at 0 MV/m is acquired following the removal of an external magnetic field $\overrightarrow{H_{in}}$ of 0.28 T. The white frames surrounding the squares highlight those with an initial magnetic vortex state (i.e., Landau states). XMCD-PEEM images taken at 0.66 MV/m shows squares with two-domain states in colored frames, suggesting successful electrically-driven transformations. The bottom row presents the statistics of squares that undergo such transformation and at what electric field. The black dotted line plots on both side of the XMCD-PEEM images record the average activation electric-field for each row of the square arrays, with the activation voltage higher towards the bottom rows.

3.4 X-ray microdiffraction analysis of the strain distribution

The induced-strain distribution across the substrate underneath the microstructures is acquired after reconstructing the arrays of Laue diffraction pattern. The reconstructed strain maps with a step size of 2 μm taken at a higher electric field is subtracted by that taken at zero electric field to yield the electrically-induced strain at that given finite electric field. The resulting strain maps of electrically-induced strain ε along [100], [01-1], [011] are shown in Figure 3.4. The induced total strain $\varepsilon_{total} = \varepsilon_{[100]} - \varepsilon_{[01\bar{1}]}$ determines the magnetoelastic uniaxial anisotropy factor $K_{m.e.}$ ($K_{m.e.} = \frac{3}{2}\lambda_s \varepsilon_{total} Y$) [53]. Since $K_{m.e.}$ drives the reorientation of magnetic moments and domains shown in Figure 3.3, the variations in total strain versus the applied electric field are also plotted in Figure 3.4 (rightmost column).

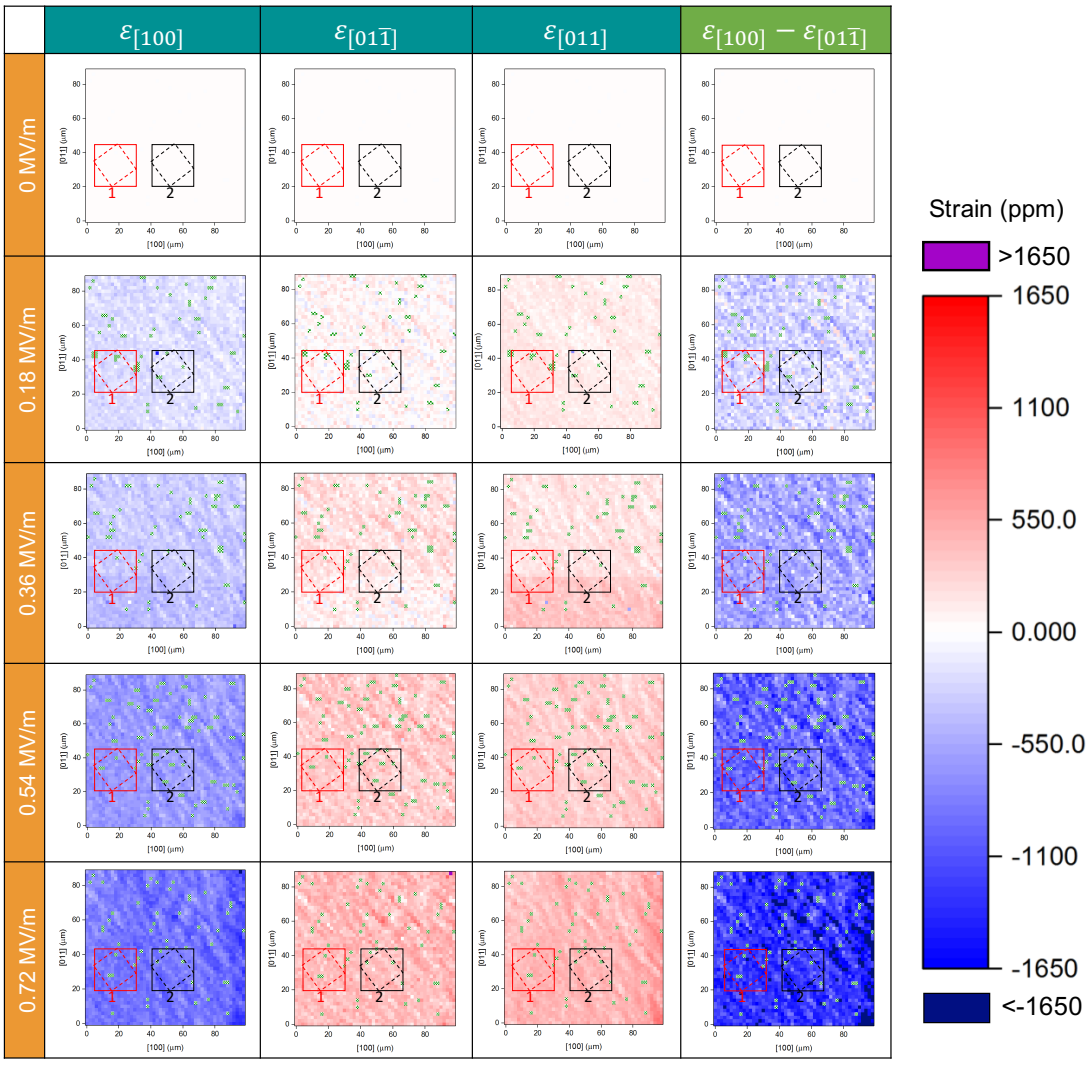

Figure 3.4. Reconstructed strain maps of the strain variation with respect to that at zero electric field along three main crystallographic orientations, [100], [01-1] and [100]. The pixel size of the images is 2x2 μm^2. The scanning area of 100x100 μm^2 (same as the region covered by Figure 3.1b) also includes the square arrays imaged by XMCD-PEEM. Missing pixels occurred during raster scan are marked in green.

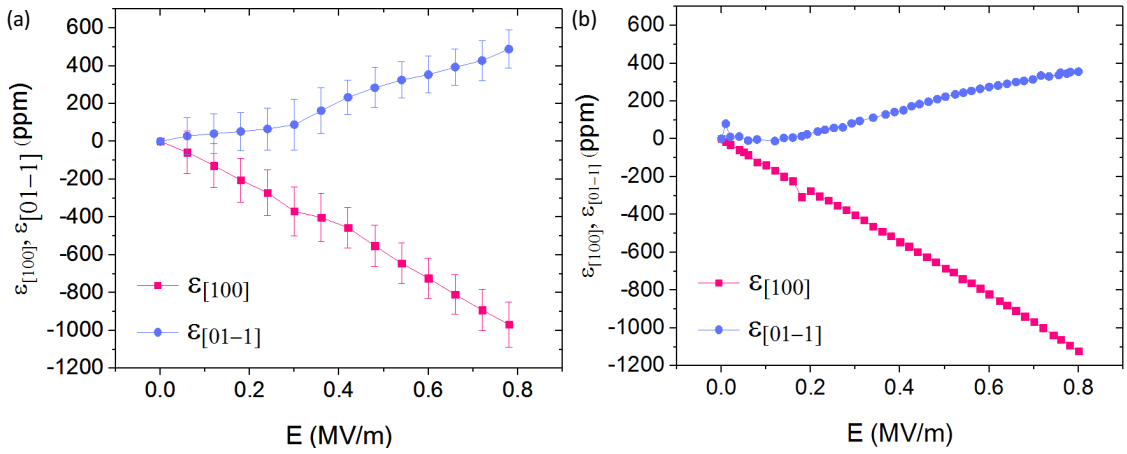

Figure 3.5. (a) Average strain in-plane along two crystallographic directions [100] and [01-1] as a function of the applied electric field. The error bar reflects the standard deviation of the strain values at all pixels, measured by x-ray microdiffraction. (b) In-plane strain along two crystallographic directions [100] and [01-1], measured by a bi-axial strain gauge. All strain values are reported in parts per million (p.p.m.).

We note that the distribution of the electrically-induced strains is spatially non-uniform at different locations in this surveyed area of 100x100 μm^2, with the strain increasing diagonally from top right to bottom left. Such strain distribution in the region of interest also explains why the activation field is in general larger for squares on the bottom rows, as shown in Figure 3.3. The resolution of the images is limited by the x-ray beam spot size and step size used during the diffraction data collection [51]. Since the resolution of the strain map is on par with the size of the magnetic microstructure (i.e., both on μm scale), we conclude that the inhomogeneous response of the initial vortex state to the electric field is affected by the non-uniform localized strain.

Even though the strain mapping with high resolution shows non-uniform electrically-induced strain across the surface, we note that the average strain values at each electric field agrees with the macroscopic strain values measured by a bi-axial strain gauge, as shown in Figure 3.5.

3.5 Concluding Remarks

In summary, we correlate the inhomogeneous magnetic behavior in microstructures to the non-uniform electrically-induced strain distribution at the surface of a ferroelectric substrate, based on XMCD-PEEM and x-ray microdiffraction studies. The information above is valuable for further understanding and manipulation of such miniaturized composite multiferroic systems.

Chapter 4 Magnetoelectric coupling in Composite Multiferroics

4.1 Introduction

The Villari effect (a.k.a., magnetoelastic effect) describes the behavior where applied mechanical stress σ produces change in the magnetization in a material [33]. Optimizing the transfer of strain and magnetic response in strain-coupled multiferroic heterostructures is key to maximizing the Villari effect, which is at the core of applications such as magnetic random access memory (MRAM), field sensors, and actuators [54, 55]. One of the main problems with laminate composites consisting of FM thin film and FE single crystal is the large "clamping" effect of the FE onto the FM film which prevents the strain effect of the FE from being exploited fully [56, 57] [58, 59].

Furthermore, as mentioned in the previous chapters, strain-mediated manipulation of magnetic behavior of Ni structures above PMN-PT have been successfully demonstrated experimentally. However, since Ni is not strongly magnetostrictive, it becomes appealing to enhance the magnetoelectric coupling in Ni/PMN-PT composite systems.

In this chapter, we report that by inserting a thin dielectric polymer layer between the FM polycrystalline Ni thin film and FE single crystal (011)-cut $[Pb(Mg_{1/3}Nb_{2/3})O_3]_{(1-x)}$-$[PbTiO_3]_x$ (PMN-PT, $x \approx 0.30$) single crystal, a nearly twofold increase in the electric field-induced FM film's variation of remanent magnetization is observed, when compared with a sample without any polymer layer. The interposed polymer not only serves as a planarization layer that smoothens the surface, but also alters the strain-mediated magnetization response of the magnetic layer in the heterostructure.

4.2 Experimental Procedure

In this study, the two FE specimens used are cut from a polished and unpoled 20 × 10 × 0.5 mm^3 single crystal, (011)-oriented $[Pb(Mg_{1/3}Nb_{2/3})O_3]_{(1-x)}$-$[PbTiO_3]_x$ (x≈ 0.30), grown by TRS Ceramics, Inc. (PA, US) following the modified Bridgman method [60]. A 5 nm Ti/50 nm Pt layer, deposited on both sides of the PMN-PT substrate, served as an adhesion layer and surface electrode, respectively [61]. For one of the specimens, adhesion promotor AP3000 and dielectric benzocyclobutene (BCB) monomer of 10 μm thick were spun onto the top electrode, followed by thermal curing in N_2 chamber at 250°C. After poling the PMN-PT substrate, 5 nm Ti/15 nm Ni films were deposited by e-beam evaporation. The purpose of poling prior to the deposition of FM layer is to reorient spontaneous polarizations, thereby reducing the ferroelastic energy [62] and prepare the substrate to work in its linear piezoelectric regime. Configurations of the two specimens are illustrated in Figure 4.1, where the crystal orientations and piezo-response of the single-crystal PMN-PT substrate, upon application of an electric field, are highlighted. The electric field applied along the [011] direction induces a large uniaxial compressive strain along the [100] direction and a reasonably small tensile strain along the [01-1] direction in the substrate.

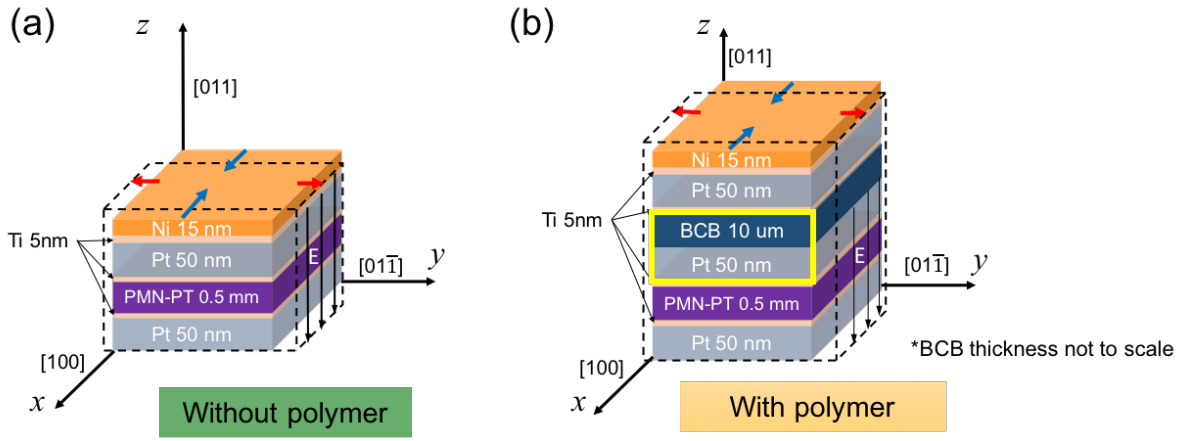

Figure 4.1 Schematics of fabricated Ni layer on (011)-oriented PMN-PT heterostructures (a) without polymer and (b) with polymer. Dashed lines outline the piezoresponse of the substrate when an electric-field is applied to the parallel plate electrode structure.

To characterize the FM layers, atomic force microscopy (AFM) images of the surfaces of Ni thin films on both specimens were collected using a Bruker Dimension icon scanning probe microscope. Bruker D8 x-ray diffraction (XRD) and high-intensity synchrotron XRD measurements of FE and FM heterostructures were obtained to confirm the crystal orientation and the structural property of Ni. In-plane piezoelectric responses were measured by attaching a biaxial strain gauge to the top surface of each of the two samples and applying an out-of-plane electric field. To compare the magnetization response of Ni thin film to the varying electric field, a longitudinal mode magneto-optical Kerr effect (MOKE) magnetometer was used. To ensure the accuracy of measurement, a Kerr hysteresis measurement was performed twice on two sets of such specimens, prepared from two 20 × 10 × 0.5 mm^3 PMN-PT substrates cut from the same crystal.

4.3 Experimental Results

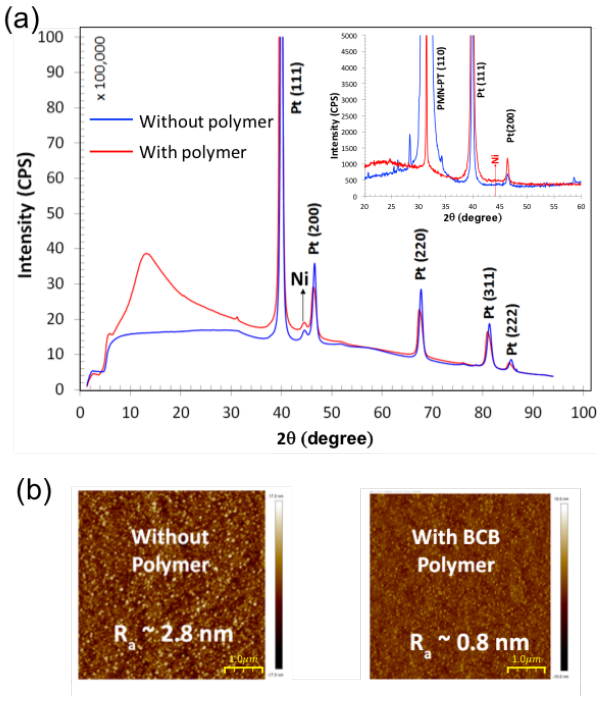

Figure 4.2. GIWAS (taken at beamline 11-3 at SSRL) patterns of two heterostructures with and without polymer layer, showing that each Ni thin film is polycrystalline in both specimens. Inset shows the powder diffraction spectra (taken on Bruker D8) of both samples, confirming the crystal orientation in PMN-PT substrate. (b) AFM topography images of Ni thin films on both samples.

With sufficient penetration depth to reach the FE substrate in both samples, XRD measurement contains information of the FE layer, as shown in the inset of Figure 4.2a. The XRD spectra indicate a strong x-ray peak corresponding to (110) orientation, confirming the crystal orientation of the PMN-PT substrate. Due to limited thickness of Ni layers and thus low intensity signals, Ni peaks are not identified in the XRD spectra shown in the inset. Therefore, synchrotron XRD with higher x-ray flux was then used. Surface XRD analysis (see Figure 4.2a) suggests that 15 nm thick Ni thin film is polycrystalline in both samples and that the BCB polymer is amorphous, as shown by the broad peak (red) between 10 and 30 degrees. Atomic force microscopy micrographs (see Figure 4.2b) of the Ni surface in both samples show that the presence of the polymer decreases the surface roughness of Ni from ~2.8 nm (without polymer) to ~0.8 nm.

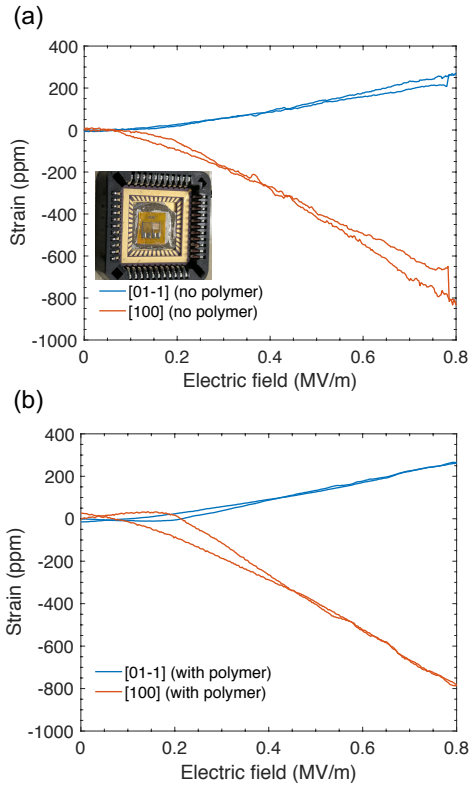

Figure 4.3. In-plane piezoelectric strain along [01-1] and [100] directions for sample (a) without polymer and (b) with polymer vs applied electric field. Inset in (a) shows a biaxial strain gauge mounted on the sample without polymer.

Figure 4.3 shows the electric-field induced strain from the poled PMN-PT substrates characterized with a biaxial strain gauge. Both unipolar strain curves, measured along [100] and [01-1] directions, are shown for both samples, indicating a linear anisotropic response that can be used to drive anisotropic magnetoelectric response in Ni layer of both samples. According to the strain response measured from both samples, we note that the transition of the strain as a function of electric field on the sample with polymer is, macroscopically speaking, of the same magnitude as that on the one without. Since the strain gauge probes the macroscopic strain response, the anisotropic strain generated by both samples are comparable, as shown in Figure 4.3(a) and (b), implying that a complete strain transfer can be achieved even with the addition of the 10 μm thick polymer.

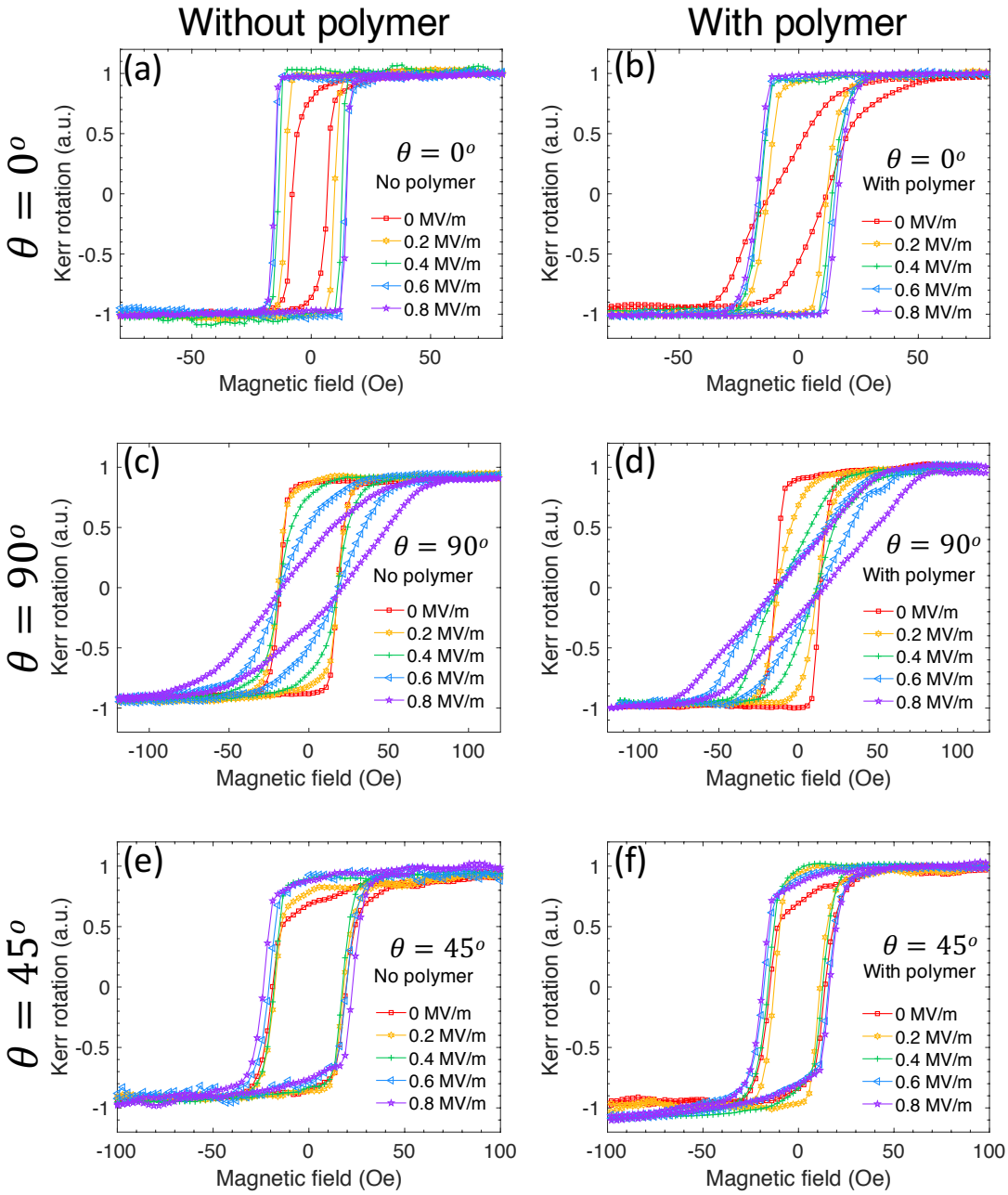

Figure 4.4. Normalized magnetic Kerr rotation M-H curves measured at different electric fields with magnetic field parallel to $\theta = 0^{o}$, $\theta = 45^{o}$ and $\theta = 90^{o}$ directions, where θ is the angle between in plane magnetic field H and [100] direction of PMN-PT. (a)(c)(e) Without polymer. (b)(d)(f) With polymer.

In the specimen with interposed polymer, the electric-field-induced strain in the PMN-PT was first transferred to the polymer and then to the top FM Ni thin film, as opposed to the direct strain transfer usually found in a PMN-PT/Ni composite system [35, 61]. To understand the difference in ME response between these two systems, in-plane magneto-

optical Kerr (MOKE) magnetometry with in-situ electric fields was employed to study M-H hysteresis loop variation for both samples. The two MOKE specimens were oriented in three directions during the experiment such that the external magnetic field was applied in the direction at an angle θ of 0^o, 90^o and 45^o with respect to the [100] direction of PMN-PT (see Figure 4.1(a)).

Figure 4.4 shows the normalized Kerr rotation hysteresis curves taken along the three directions mentioned above. Before applying an electric field, negative magnetostrictive Ni on the pre-poled substrate is found to have a magnetic easy direction along [01-1] direction and a hard direction along [100] direction, as shown in Figure 4.4(a)-(d). Comparing Figure 4.4(a) and (b) showing MOKE M vs H curve for samples without and with polymer, respectively, we note that the presence of the planarization polymer increases the hard-axis anisotropy and thus reduces the remanence-saturation ratio M_r/M_s (normalized remanence). The M_r/M_s measured at an electric field of 0 MV/m in the specimen without polymer is greater than 0.85, while in the specimen with polymer it is below 0.45.

As the electric field increases from 0 MV/m to 0.8 MV/m, the increasingly large anisotropic strain generates a new magneto-elastic uni-axial anisotropy term along the [100] direction. As a result, the magnetic easy-axis rotates from 90° to 0^o. i.e., the [100] direction switches from being the hard to the easy axis, and [01-1] from the easy to the hard. M-H curves taken along [100] for both samples show a clear inverse ME effect (Villari effect) with significant strain transfer to the FM. However, in the composite system with a smooth polymer layer, the variation of M_r/M_s as a function of the electric field is more prominent compared to the one without polymer, as shown in Figure 4.5, for cases where magnetic field is applied along θ of 0^o and 90^o. Hence, the ME coupling between magnetic thin film and PMN-PT grows stronger due to the presence of the interposed polymer layer, as shown by the almost two-fold increase in M_r/M_s (θ of 0^o) before and after applying the electric field of 0.8

MV/m. The presence of the polymer layer smoothes the strain profile and planarizes the Ni layer, indicating an increased magnetoelastic effect.

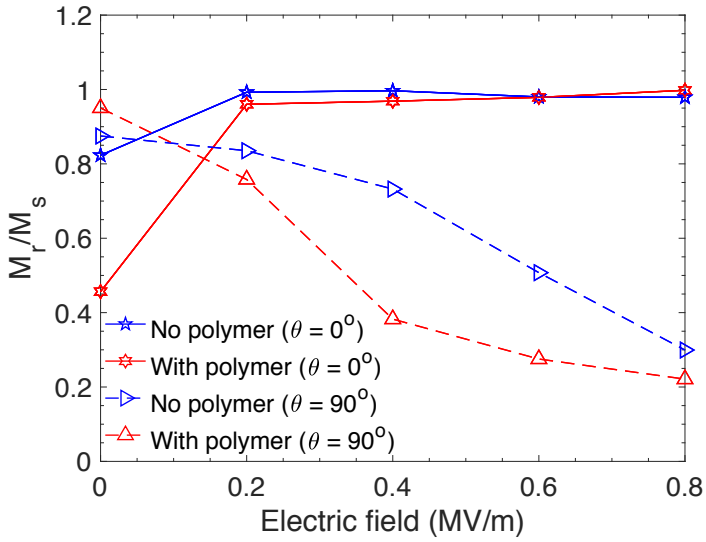

Figure 4.5. M_r/M_s, as a function of the applied electric field, for both samples. The magnetic field direction is parallel to $\theta = 0^o$ and $\theta = 90^o$. A larger change in M_r/M_s vs electric field is observed in both directions for the sample with polymer than the one without.

Additionally, for magnetic field applied along 45^o, bisecting the alternating easy and hard axes, the shape of hysteresis loops remains consistent as the electric field varies. Magnetic moments pointing along this direction are unlikely to change direction as the electric field changes.

When the electric field is ramped down from 0.8 MV/m to 0 MV/m, the magnetization state of Ni film is reversible in both specimens, where the M-H loop overlaps with the one measured at the same electric field while ramping up the voltage. Figure 4.6 demonstrates the reversibility of the magnetic behavior in Ni thin film on the polymer layer, with magnetic hysteresis loops measured along [100] direction. Repeatable magnetization states can be switched by electric fields, as shown in Figure 4.6 at 0 MV/m, 0.4 MV/m and 0.8 MV/m. For both samples, overlapping of M-H loops, taken when the same electric fields were applied, also verifies the accuracy of the MOKE measurements.

Such enhanced magnetoelectric coupling are believed to originate from several sources. First, the presence of polymer modifies the magnetic property of the Ni thin film deposited on the pre-poled substrates such that along θ of 0^o direction, the anisotropy field is larger in the sample compared to the one without polymer. With increased electric field, the thin film in the sample with polymer experiences a stronger change in M_r/M_s, in other words, a larger variation in $\Delta(M_r/M_s)/\Delta E$. Second, the planarization layer smoothens the interface between Ni and substrate. Compared to the sample without polymer where the Ni and Pt interface has grain boundaries, the sample with polymer reduces pinning effect due to lower surface roughness. As a result, the magnetic property of Ni can be largely affected, thus contributing to difference in the magnetoelectric properties of the two specimens. The addition of such polymer layer introduces a new degree of freedom of magnetization control in strain-mediated multiferroic systems.

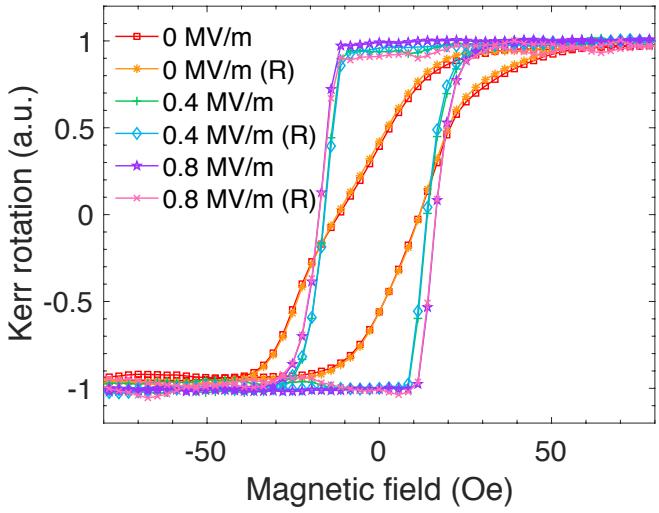

Figure 4.6. Reversible magnetic behavior of the Ni thin film in the specimen with interposed polymer layer, measured along [100] direction. Where "R" denotes the M-H loop taken as the electric field was ramped down from 0.8 MV/m to 0 MV/m.

4.4 Concluding remarks

In summary, we have shown that by interposing a polymer layer in strain-mediated multiferroic structures, enhancement of the magnetoelectric coupling can be achieved. Switching electric-field to operate the (011)-oriented PMN-PT (PT% ≈ 0.30) in the linear regime drives magnetization response in Ni thin films. The Ni thin film above the polymer exhibits an improved sensitivity of remanence to anisotropic strain originating from PMN-PT. Such interposed polymer layer provides an additional pathway to control and enhance the magnetoelectric coupling in composite multiferroic devices.

Chapter 5 Summary and Outlook

5.1 Research Summary

In the last decade, composite multiferroic systems have been attracting an increasing interest due to their potential applications in energy-efficient multi-functional devices. Electric-field control of magnetism subsequently emerges as a promising method to be used in future technological applications, such as memory, nanoscale actuators, and microfluidics manipulation, etc. In this thesis, we have focused on the two main components of one type of such multiferroic heterostructure, including the coupling behaviour between magnetic moments and electrically-induced strain from both modelling and experimental perspectives, and a method of enhancing the coupling behaviour between the two components.

5.2 Outlook and Prospect

Although the working principles and physics of energy-efficient strain-mediated multiferroic heterostructures have been studied, more work needs to be done. For example, we need to improve the uniformity of the microstructure performance across the device, and lower the electric-field required for actuating the change in magnetization, either in the form of domain rotation or magnetization direction switching. Materials with high magnetostriction such as Terfenol-D and Galfenol ($Fe_{81}Ga_{19}$ alloys) could potentially be a good replacement of Nickel. Furthermore, we can look into suitable application of our miniaturized device in domains such as automated cell sorting with individual cell addressability in lieu of current cell sorting method (e.g., MACS (magnetic-activated cell sorting), etc.).

APPENDICES

Appendix A. Initial Magnetization Classification

For nanoscale magnetic structures, it is mainly the competition between magnetic anisotropies and the geometry of the structures that determines the initialization state at the equilibrium, which relaxes from the saturated initial state, where all individual magnetic moments throughout the ring point towards +*x*-direction (Figure 2.1b) [63]. During relaxation from the saturated initial state, the competition between exchange energy and magnetostatic energy (i.e., demagnetization energy) plays a pivotal role for total energy minimization in the magnetic structure. The micromagnetic simulation model can be simplified for characterizing the dependence of the initial mapping of domain states on the ring dimensions. For obtaining initial mapping of domain states, we only consider the dominant energy terms, i.e., exchange energy and magnetostatic energy, from the Landau-Lifshitz-Gilbert (LLG) equation [64]. In this way, such initial remanent states for various ring geometries can be approximated using micromagnetics alone.

To find the magnetic ground state in the magnetoelastic rings, we use OOMMF micromagnetic simulator to identify domain states attainable in rings with outer diameter (*OD*) on micron scale, width (*w*) and thickness (*t*) on submicron scale. According to previous investigation on Ni rings, at relaxation states after initialization, these submicron size scales rings are capable of achieving an "onion state" with either transverse DWs or vortex DWs on opposite sides of the ring, and a vortex state with flux closure domains around the ring [3]. DW states at equilibrium in Terfenol-D rings with different dimensions have been modeled using the OOMMF micromagnetic simulation with an initial magnetization all aligned in +*x* direction [65].

In this work, we simulated nanoscale rings with a variety of dimensions, including rings with *OD* of 1 μm, *w* of 50 nm, 150 nm, 300 nm, and 400 nm, and *t* of 15 nm, 30 nm and 45 nm, along with rings with *OD* of 2 μm, *w* of 150 nm, 300 nm, 400 nm, 600 nm, and *t* of 15 nm, 30 nm and 45 nm. Correlation between energy density and magnetic configurations in those ring structures is further examined to produce phase diagrams with design specifications for rings with geometries that are energetically favorable for the desired onion states [64, 66].

The relevant length scales for the ring structure are the *OD, w, t* and the magnetostatic exchange length l_{ex} expressed as $l_{ex} = \sqrt{\frac{2A}{\mu_0 M_s^2}}$, where A is the exchange stiffness, and M_s is the saturation magnetization.[66] For Terfenol-D, the calculation is performed based on the following parameters, A = 1.0 ×10^{-11} J/m and M_s = 8.0 × 10^5 A/m, giving $l_{ex} = 5.0$ nm [67].

For the micromagnetic model, the maximum $d\mathbf{m}/dt$ is set as 0.02 for a more precise simulation of domain states in Terfenol-D ring structures with *OD* of 1 μm and 2 μm. Due to the competition between demagnetization and exchange energies, the magnetic ring states vary from onion states to vortex state with a flux closure configuration when the ring's width is increased. Onion states with transverse DWs are of interest due to their large energy density and stray field. The energy flux out of the ring can have practical applications in trapping and/or interacting with nano- and micro-scale particles in the surroundings of the ring via localized magnetostatic interaction [68]. Depending on the ring dimension and *w/OD* ratio, the magnetic energy density of rings with the same *OD* versus thickness of the ring are plotted in Figure A1a-b. Magnetic domain states associated with some of the representative data points are also shown in the plot. Figure S1a shows the magnetic energy density and equilibrium magnetic states after initialization for rings with *OD* of 1 μm and Figure S1b shows these for rings with *OD* of 2 μm. For rings with fixed *OD* of 1 μm and *t* of 45 nm, the

increase in ring width leads to DW configuration changing from vortex domain onion state to vortex onion state for magnetic energy minimization of the rings. In the cases with fixed *OD* of 1 µm and *w* of 300 nm, as *t* increases from 15 nm to 30 nm, and 45 nm, domain configuration changes from transverse domain onion state to vortex state, as shown in Figure S1a. Similarly, as shown by the domain configurations in Figure A1b, increase in *t* from 15 nm to 45 nm shows domain state transitioning from transverse domain onion state to vortex domain onion state for Terfenol-D rings with 2 µm in diameter. Calculation of ring energy density and categorization of domain states result in partial phase diagrams for Terfenol-D rings, as shown in Figure A1c-d [64]. The phase diagram which suggests various forms of domain states at equilibrium following initialization, depending on the ring dimensions, is particularly useful for the experimental design of Terfenol-D rings.

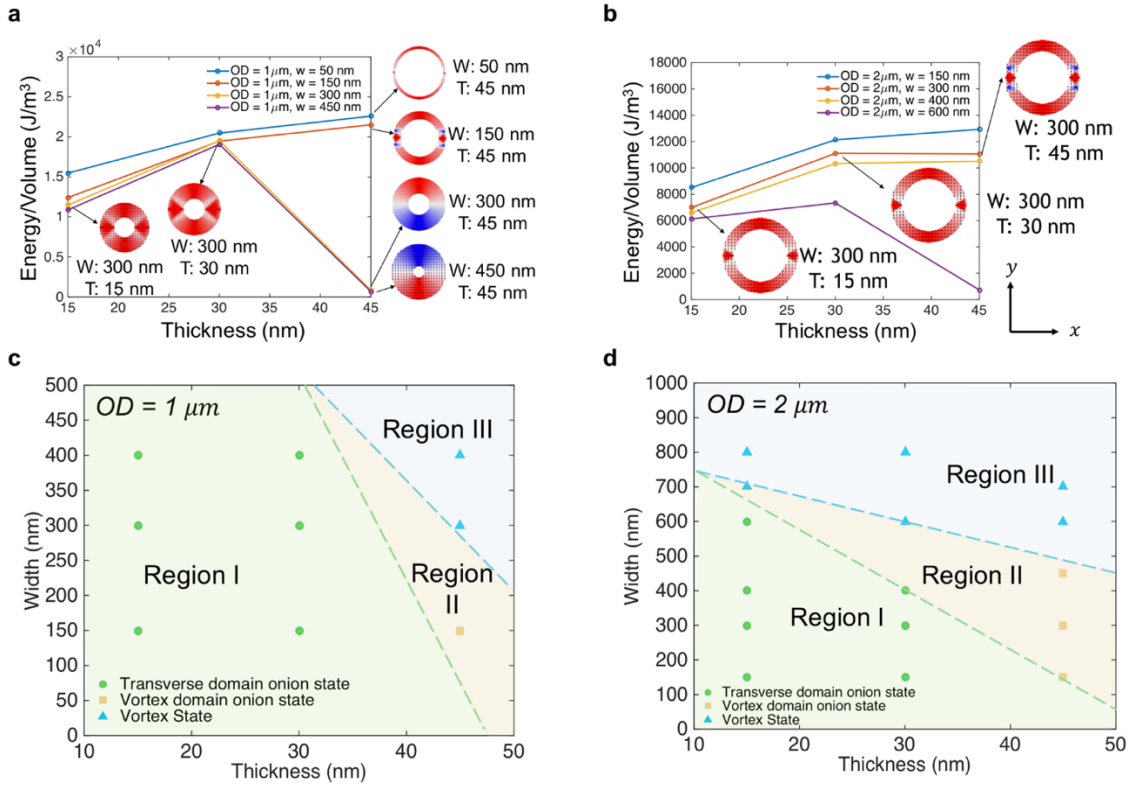

Figure A1. Magnetic energy density (as determined by micromagnetic modeling) vs. Terfenol-D ring's thickness. Each ring structure shows its final magnetic domain state (with spin structure) at equilibrium after initializing all magnetic moments in the +*x* direction and

allowing them to relax to equilibrium. (a) Rings with *OD* of 1 μm. (b) Rings with *OD* of 2 μm. (c)-(d) Calculation of the DW energies gives rise to a proposed phase diagram for DW transition with respect to the ring dimensions (ring width *w* versus thickness *t*) for both (c) *OD* of 1 μm rings, and (d) *OD* of 2 μm rings.

Appendix B. Equivalent coupled model setup

To reduce simulation time while maintaining accurate results, the multiphysics finite element model can also be set up with a Terfenol-D or Ni ring on top of a SiO_2 substrate, as shown in Figure B1. This separates the computation required for piezoelectric strain to a separate modeling step. Tensile strain is then induced along 45^o in the counter clockwise direction away from the +*x* axis, and compressive strain along -45^o to the +*x* axis. Therefore, for Terfenol-D with positive magnetostriction, magnetization and DWs tend to orient along 45^o away from the +*x* axis (i.e., along tensile strain direction), same DW behavior as on PMN-PT substrate.

The purpose of choosing a thickness of 500 nm for the substrate rather than a few hundred of microns to match PMN-PT substrate thickness is to make the computations feasible while not affecting the results.

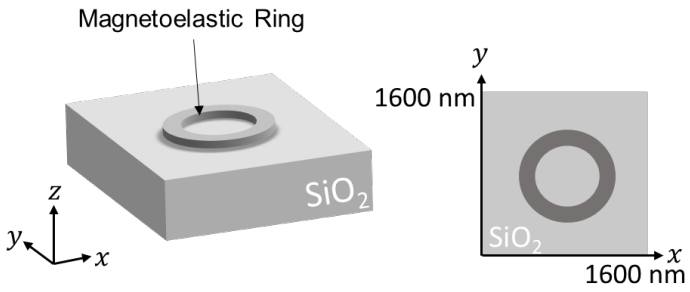

Figure B1. Geometry of the setup in COMSOL Multiphysics, where strain is applied to SiO_2 substrate to achieve similar effect as applying voltage to the piezoelectric substrate.

Appendix C. Bi-directional coupled model with varied parameters

Note C1 Influence of ramping speed on the domain wall dynamics

The speed of ramping electric field/ strain can affect the domain wall rotation dynamics. Strain of different amplitudes are applied to the substrate with the following ramping slopes k = 10^{10} s^{-1}, 10^{9} s^{-1}, and 10^{8} s^{-1}, and the corresponding time for ramping t is 0.1 ns, 1 ns and 10 ns. Here, we show the average magnetization angle rotation dynamics predicted by bidirectional model for Terfenol-D ring with an applied strain of 500 ppm (as shown in Figure C1). By comparison, we conclude that the ramping slope of the electric field/strain affects the dynamics of the system, but can lead to similar magnetization states in the ring at equilibrium following the application of strain for this case.

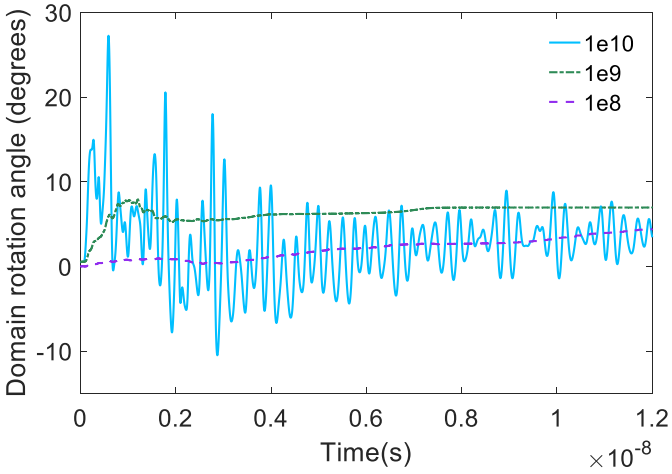

Figure C1. Domain wall angle as a function of strain application time in Terfenol-D rings calculated by bidirectional models, with a strain of 500 ppm generated in the substrate.

Note C2 Influence of mesh size and time step on convergence

To compare the effect of mesh size and time step on convergence, we used the BD model to predict magnetization variation in the Terfenol-D ring when a 1000 ppm strain is applied. The model setup that produces the result in the main text adopts a mesh size of 10 nm for the ring, and 40 nm for the substrate. A model with much finer mesh element setup has a mesh size of 5 nm (close to the exchange length in Terfenol-D) for the ring, and 10 nm for the substrate. The time step is taken as 5 ps for the first model, and 1ps for the second model. As

shown in Figure C2, magnetization rotation predicted by the BD model with larger mesh size (Figure C2, left) predicts the same tendency as modeled by the BD model with smaller mesh size (Figure C2, right). With a dramatically increased number of mesh elements, the latter model obtains better convergence during simulation (convergence error below 10^{-1}), while still following the same domain rotation trend as predicted by the one adopted in the letter. In addition, **Figure C3** shows the magnetization configurations in Terfenol-D ring predicted by both models at equilibrium. We thus conclude that the finest mesh size used here is not necessary as it is much more time-consuming and differs little from the ones using larger mesh size. The model used for the letter is sufficient to describe the overall magnetization dynamics in the systems.

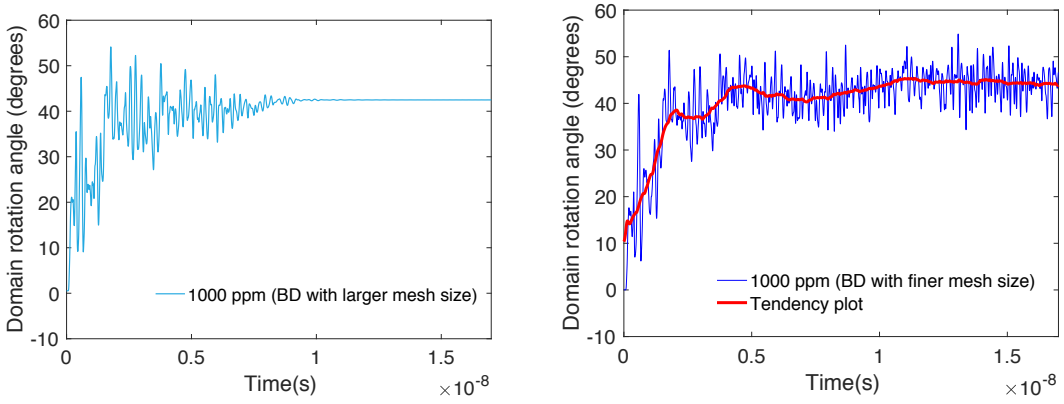

Figure C2. Comparison of domain rotation dynamics predicted by BD model when 1000 ppm strain is applied to the piezoelectric substrate. The plot on the left, shown in the main text of the paper, uses a larger mesh size (10 nm for Terfenol-D, 40 nm for substrate) and a time step of 5 ps. The plot on the right uses a finer mesh size (5 nm for Terfenol-D, 10 nm for substrate) and a time step of 1 ps.

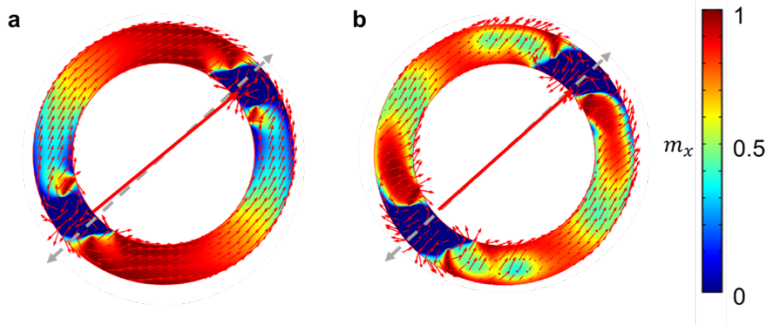

Figure C3. Comparison of the magnetization states in Terfenol-D ring modeled with different mesh sizes at 18 ns. (a) Domain wall rotation angle at 42o, considered as full rotation, predicted by the BD model setup used in the main text of the letter. (b) Domain rotation angle at 42o, considered as full rotation, predicted by the BD model with smaller mesh size, corresponding to Figure S4 (right)

Appendix D. Effect of polymer on lowering the electric-field activation threshold

Here, we show the effect of the polymer layer on lowering the electric field which triggers magnetic domain wall motion in lithographically fabricated Ni micro-rings. To visualize the influence of the interposed polymer layer, lithographically patterned Ni rings, which have an outer diameter of 2 μm and thickness of 15 nm (5 nm Ti/ 15nm Ni), rather than Ni thin films, are grown directly onto the polymer via e-beam evaporation and lift-off.

X-ray magnetic circular dichroism photoemission electron microscopy (XMCD-PEEM) was performed at the Advanced Light Source at Lawrence Berkeley National Laboratory. XMCD-PEEM with in-situ electric field applied across the substrate probed the electrically-driven domain wall rotation in the Ni rings.

The XMCD-PEEM images of a Ni ring on polymer are to be compared and contrasted with a Ni ring, with an outer diameter of 2 μm and thickness of 30 nm (5 nm Ti/ 30 nm Ni), grown directly on the top surface electrode, which was previously reported by Sohn et al. [35]Moreover, the variation of magnetic states in the Ni ring structures of comparable

dimensions on PMN-PT substrates with and without polymer can be obtained and compared using XMCD-PEEM imaging.

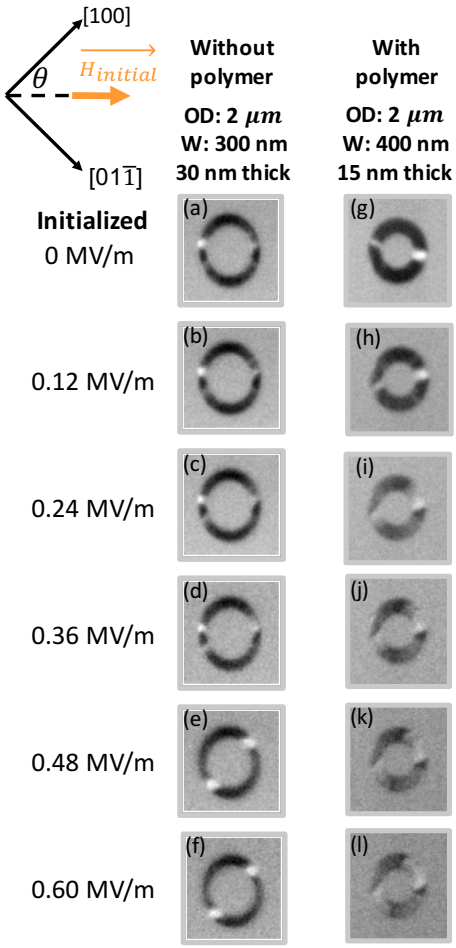

Figure D1. XMCD-PEEM images of electric-field driven domain wall motion in Ni ring structures. Onion state domain movement in multiferroic heterostructures (a)-(f) without polymer, (g)-(l) with polymer. (a) and (f) are adapted in part with permission from Sohn et al. [35] Copyright (2015) American Chemical Society.

First, the selected ring dimensions formed onion states after initializing with a 3 kOe external magnetic field applied at θ = 45^{o}, which is similar to the initial onion state of Ni rings in heterostructures without polymer layer, as reported in Sohn et al[35]. Supplementary Figure D1 shows the PEEM images for both Ni rings on PMN-PT without polymer (see Figure D1(a)-(f)) and with polymer (see Figure D1(g)-(l)).

The Ni rings are both 2 μm in outer diameter (OD) and can both form onion states after removing the magnetic field. Compared to the onion state domain rotation in Figure D1(a)-(f), the domain wall movement becomes initiated at a lower electric field Figure D1(g)-(l). In addition to what have been shown in the MOKE magnetometry measurements for Ni thin film layers, the Ni thin rings with localized magnetization variation also suggest that the interposed polymer layer alters the local strain profile as seen by the FM layer, and its presence alters the magnetoelastic coupling behavior between the FE PMN-PT to FM Ni structures.

It is noted that the outer diameters of the rings with and without polymer are the same, but the inner diameter and thickness are not. While these differences prevent an exact comparison of the case with and without polymer, the early onset of domain broadening of the rings with polymer is a further point supporting the idea that the polymer layer enhances magnetoelectric coupling in the nanoscale rings.

REFERENCE

[1] M. F. Nicola A. Spaldin, "<Renaissance of Magnetoelectric Multiferroics_science.pdf>," *Science,* vol. 309, pp. 391-392, 15 Jul 2005. 2005.

[2] W. Eerenstein, N. D. Mathur, and J. F. Scott, "Multiferroic and magnetoelectric materials," *Nature,* vol. 442, pp. 759-65, Aug 17 2006.

[3] H. Sohn, M. E. Nowakowski, C. Y. Liang, J. L. Hockel, K. Wetzlar, S. Keller*, et al.*, "Electrically Driven Magnetic Domain Wall Rotation in :Multiferroic Heterostructures to Manipulate Suspended On-Chip Magnetic Particles," *Acs Nano,* vol. 9, pp. 4814-4826, May 2015.

[4] S. S. P. Parkin, M. Hayashi, and L. Thomas, "Magnetic domain-wall racetrack memory," *Science,* vol. 320, pp. 190-194, Apr 11 2008.

[5] T. Taniyama, "Electric-field control of magnetism via strain transfer across ferromagnetic/ferroelectric interfaces," *Journal of Physics: Condensed Matter,* vol. 27, 2015.

[6] A. B. C.Chen, A. Mal, G. Carman and A. Sepulveda, "Voltage induced mechanical/spin wave propagation over long distances," *Applied Physics Letters,* vol. 110, 2017.

[7] Y. C. Xiaobin Wang, Ying Gu, Hai Li, "Spintronic Memristor Temperature Sensor," *IEEE Electron Device Letters* vol. 31, pp. 20 - 22

[8] J. Cui, J. L. Hockel, P. K. Nordeen, D. M. Pisani, C.-y. Liang, G. P. Carman*, et al.*, "A method to control magnetism in individual strain-mediated magnetoelectric islands," *Applied Physics Letters,* vol. 103, p. 232905, 2013.

[9] C. H. A. Trifon M. Liakopoulos, "A micro-fluxgate magnetic sensor using micromachined planar solenoid coils," *Sensor and Actuators* pp. 66-72, 1999.

[10] L. E. Helseth, T. M. Fischer, and T. H. Johansen, "Domain wall tip for manipulation of magnetic particles," *Phys Rev Lett,* vol. 91, p. 208302, Nov 14 2003.

[11] T. H. Lahtinen, K. J. Franke, and S. van Dijken, "Electric-field control of magnetic domain wall motion and local magnetization reversal," *Sci Rep,* vol. 2, p. 258, 2012.

[12] A. K. Biswas, S. Bandyopadhyay, and J. Atulasimha, "Complete magnetization reversal in a magnetostrictive nanomagnet with voltage-generated stress: A reliable energy-efficient non-volatile magneto-elastic memory," *Applied Physics Letters,* vol. 105, Aug 18 2014.

[13] J. M. Hu, T. Yang, J. Wang, H. Huang, J. Zhang, L. Q. Chen*, et al.*, "Purely electric-field-driven perpendicular magnetization reversal," *Nano Lett,* vol. 15, pp. 616-22, Jan 14 2015.

[14] J. M. Hu, L. Q. Chen, and C. W. Nan, "Multiferroic Heterostructures Integrating Ferroelectric and Magnetic Materials," *Adv Mater,* vol. 28, pp. 15-39, Jan 6 2016.

[15] X. Li, D. Carka, C. Y. Liang, A. E. Sepulveda, S. M. Keller, P. K. Amiri*, et al.*, "Strain-mediated 180 degrees perpendicular magnetization switching of a single domain multiferroic structure," *Journal of Applied Physics,* vol. 118, Jul 7 2015.

[16] A. Morelli, F. Johann, S. R. Burns, A. Douglas, and J. M. Gregg, "Deterministic Switching in Bismuth Ferrite Nanoislands," *Nano Lett,* vol. 16, pp. 5228-34, Aug 10 2016.

[17] N. D'Souza, M. S. Fashami, S. Bandyopadhyay, and J. Atulasimha, "Experimental Clocking of Nanomagnets with Strain for Ultralow Power Boolean Logic," *Nano Letters,* vol. 16, pp. 1069-1075, Feb 2016.

[18] R. C. Peng, J. M. Hu, K. Momeni, J. J. Wang, L. Q. Chen, and C. W. Nan, "Fast 180 degrees magnetization switching in a strain-mediated multiferroic heterostructure driven by a voltage," *Sci Rep,* vol. 6, p. 27561, 2016.

[19] M. Weiler, A. Brandlmaier, S. Geprägs, M. Althammer, M. Opel, C. Bihler*, et al.*, "Voltage controlled inversion of magnetic anisotropy in a ferromagnetic thin film at room temperature," *New Journal of Physics,* vol. 11, p. 013021, 2009.

[20] J. L. Hockel, A. Bur, T. Wu, K. P. Wetzlar, and G. P. Carman, "Electric field induced magnetization rotation in patterned Ni ring/Pb(Mg1/3Nb2/3)O3](1−0.32)-[PbTiO3]0.32 heterostructures," *Applied Physics Letters,* vol. 100, p. 022401, 2012.

[21] M. Foerster, F. Macia, N. Statuto, S. Finizio, A. Hernandez-Minguez, S. Lendinez*, et al.*, "Direct imaging of delayed magneto-dynamic modes induced by surface acoustic waves," *Nat Commun,* vol. 8, p. 407, Sep 01 2017.

[22] S. Zhang, Y. Zhao, X. Xiao, Y. Wu, S. Rizwan, L. Yang*, et al.*, "Giant electrical modulation of magnetization in Co40Fe40B20/Pb(Mg1/3Nb2/3)0.7Ti0.3O3(011) heterostructure," *Sci Rep,* vol. 4, p. 3727, 2014.

[23] H. Ahmad, J. Atulasimha, and S. Bandyopadhyay, "Reversible strain-induced magnetization switching in FeGa nanomagnets: Pathway to a rewritable, non-volatile, non-toggle, extremely low energy straintronic memory," *Sci Rep,* vol. 5, p. 18264, 2015.

[24] K. P. Mohanchandra, S. V. Prikhodko, K. P. Wetzlar, W. Y. Sun, P. Nordeen, and G. P. Carman, "Sputter deposited Terfenol-D thin films for multiferroic applications," *AIP Advances,* vol. 5, p. 097119, 2015.

[25] G. Dewar, "Effect of the large magnetostriction of Terfenol-D on microwave transmission," *Journal of Applied Physics,* vol. 81, p. 5713, 1997.

[26] J. Ryu, S. Priya, A. V. Carazo, K. Uchino, and H.-E. Kim, "Effect of the Magnetostrictive Layer on Magnetoelectric Properties in Lead Zirconate Titanate/Terfenol-D Laminate Composites," *Journal of the American Ceramic Society,* vol. 84, pp. 2905-2908, 2001.

[27] S. Dong, J. Cheng, J. F. Li, and D. Viehland, "Enhanced magnetoelectric effects in laminate composites of Terfenol-D/Pb(Zr,Ti)O[sub 3] under resonant drive," *Applied Physics Letters,* vol. 83, p. 4812, 2003.

[28] Y. Jia, S. W. Or, H. L. W. Chan, X. Zhao, and H. Luo, "Converse magnetoelectric effect in laminated composites of PMN–PT single crystal and Terfenol-D alloy," *Applied Physics Letters,* vol. 88, p. 242902, 2006.

[29] R. P. P. Beardsley, D. E.; Zemen, J.; Bowe, S.; Edmonds, K. W.; Reardon, C.; Maccherozzi, F.; Isakov, I.; Warburton, P. A.; Campion, R. P.; Gallagher, B. L.; Cavill, S. A.; Rushforth, A. W., "Effect of lithographically-induced strain relaxation on the magnetic domain configuration in microfabricated epitaxially grown Fe81Ga19," *eprint arXiv:1609.02930,* 09/2016 2016.

[30] M. M. A.-R. Dhritiman Bhattacharya, Noel D'Souza, Supriyo Bandyopadhyay, Jayasimha Atulasimha, "Incoherent magnetization dynamics in strain mediated switching of magnetostrictive nanomagnets," 2015.

[31] R. P. Beardsley, S. Bowe, D. E. Parkes, C. Reardon, K. W. Edmonds, B. L. Gallagher, *et al.*, "Deterministic control of magnetic vortex wall chirality by electric field," *Sci Rep,* vol. 7, p. 7613, Aug 08 2017.

[32] A. K. Biswas, H. Ahmad, J. Atulasimha, and S. Bandyopadhyay, "Experimental Demonstration of Complete 180 degrees Reversal of Magnetization in Isolated Co Nanomagnets on a PMN-PT Substrate with Voltage Generated Strain," *Nano Lett,* vol. 17, pp. 3478-3484, Jun 14 2017.

[33] E. Villari, "Change of magnetization by tension and by electric current," *Ann. Phys. Chem,* vol. 126, pp. 87-122, 1865.

[34] J. M. Hu, T. Yang, K. Momeni, X. Cheng, L. Chen, S. Lei, *et al.*, "Fast Magnetic Domain-Wall Motion in a Ring-Shaped Nanowire Driven by a Voltage," *Nano Lett,* vol. 16, pp. 2341-8, Apr 13 2016.

[35] H. Sohn, M. E. Nowakowski, C. Y. Liang, J. L. Hockel, K. Wetzlar, S. Keller, *et al.*, "Electrically driven magnetic domain wall rotation in multiferroic heterostructures to manipulate suspended on-chip magnetic particles," *ACS Nano,* vol. 9, pp. 4814-26, May 26 2015.

[36] I. Gilbert, A. C. Chavez, D. T. Pierce, J. Unguris, W. Y. Sun, C. Y. Liang, *et al.*, "Magnetic microscopy and simulation of strain-mediated control of magnetization in Ni/PMN-PT nanostructures," *Appl Phys Lett,* vol. 109, Oct 2016.

[37] E. Rapoport and G. S. D. Beach, "Dynamics of superparamagnetic microbead transport along magnetic nanotracks by magnetic domain walls," *Applied Physics Letters,* vol. 100, p. 082401, 2012.

[38] Q. Ramadan, V. Samper, D. Poenar, and C. Yu, "Magnetic-based microfluidic platform for biomolecular separation," *Biomed Microdevices,* vol. 8, pp. 151-8, Jun 2006.

[39] C. Y. Liang, S. M. Keller, A. E. Sepulveda, A. Bur, W. Y. Sun, K. Wetzlar*, et al.*, "Modeling of magnetoelastic nanostructures with a fully coupled mechanical-micromagnetic model," *Nanotechnology,* vol. 25, p. 435701, Oct 31 2014.

[40] J. M. Hu, L. Shu, Z. Li, Y. Gao, Y. Shen, Y. H. Lin*, et al.*, "Film size-dependent voltage-modulated magnetism in multiferroic heterostructures," *Philos Trans A Math Phys Eng Sci,* vol. 372, p. 20120444, Feb 28 2014.

[41] J. X. Zhang and L. Q. Chen, "Phase-field microelasticity theory and micromagnetic simulations of domain structures in giant magnetostrictive materials," *Acta Materialia,* vol. 53, pp. 2845-2855, May 2005.

[42] Multiphysics, "C.COMSOL Multiphysics," ed. http://comsol.com/, 2015.

[43] H. F. Kronmuller, M. , *Micromagnetism and the Microstructure of Ferromangnetic Solids*, 2003.

[44] J. Walowski, M. D. Kaufmann, B. Lenk, C. Hamann, J. McCord, and M. Münzenberg, "Intrinsic and non-local Gilbert damping in polycrystalline nickel studied by Ti : sapphire laser fs spectroscopy," *Journal of Physics D: Applied Physics,* vol. 41, p. 164016, 2008.

[45] J. M. Hu, Z. Li, L. Q. Chen, and C. W. Nan, "High-density magnetoresistive random access memory operating at ultralow voltage at room temperature," *Nat Commun,* vol. 2, p. 553, Nov 22 2011.

[46] D. B. Gopman, J. W. Lau, K. P. Mohanchandra, K. Wetzlar, and G. P. Carman, "Determination of the exchange constant of Tb0.3Dy0.7Fe2 by broadband ferromagnetic resonance spectroscopy," *Phys Rev B,* vol. 93, Feb 01 2016.

[47] Y. C. Shu, M. P. Lin, and K. C. Wu, "Micromagnetic modeling of magnetostrictive materials under intrinsic stress," *Mechanics of Materials,* vol. 36, pp. 975-997, 2004.

[48] T. L. Gilbert, "Classics in Magnetics A Phenomenological Theory of Damping in Ferromagnetic Materials," *IEEE Transactions on Magnetics,* vol. 40, pp. 3443-3449, 2004.

[49] X. M. Cheng and D. J. Keavney, "Studies of nanomagnetism using synchrotron-based x-ray photoemission electron microscopy (X-PEEM)," *Rep Prog Phys,* vol. 75, p. 026501, Feb 2012.

[50] M. Buzzi, R. V. Chopdekar, J. L. Hockel, A. Bur, T. Wu, N. Pilet*, et al.*, "Single domain spin manipulation by electric fields in strain coupled artificial multiferroic nanostructures," *Phys Rev Lett,* vol. 111, p. 027204, Jul 12 2013.

[51] M. Kunz, N. Tamura, K. Chen, A. A. MacDowell, R. S. Celestre, M. M. Church*, et al.*, "A dedicated superbend x-ray microdiffraction beamline for materials, geo-, and environmental sciences at the advanced light source," *Rev Sci Instrum,* vol. 80, p. 035108, Mar 2009.

[52] R. S. Alex Hubert, *Magnetic Domains: The Analysis of Magnetic Microstructures*. Berlin: Springer, 1998.

[53] R. C. O'Handley. USA: John Wiley & Sons, Inc. Scientific, Technical, and Medical Division, 2000.

[54] Z. Jian-Gang, "Magnetoresistive Random Access Memory: The Path to Competitiveness and Scalability," *Proceedings of the IEEE,* vol. 96, pp. 1786-1798, 2008.

[55] M. Fiebig, "Revival of the magnetoelectric effect," *Journal of Physics D: Applied Physics,* vol. 38, pp. R123-R152, 2005.

[56] M. Al Ahmad, R. Coccetti, and R. Plana, "The Effect of Substrate Clamping on Piezoelectric Thin-Film Parameters," *2007 Asia Pacific Microwave Conference, Vols 1-5,* pp. 946-949, 2007.

[57] S. Zhang, "Electric-Field Control of Magnetization and Electronic Transport in Ferromagnetic:Ferroelectric Heterostructures Thesis," PhD Doctoral, Tsinghua University, Springer, 2014.

[58] R. N. Torah, S. P. Beeby, and a. N. M. White, "Experimental investigation into the effect of substrate clamping on the piezoelectric behavior of PZT," *J. Phys. D: Appl. Phys.,* pp. 1073-1078, 2004.

[59] C. W. Nan, G. Liu, Y. Lin, and H. Chen, "Magnetic-field-induced electric polarization in multiferroic nanostructures," *Phys Rev Lett,* vol. 94, p. 197203, May 20 2005.

[60] Z.-W. Yin, H.-S. Luo, P.-C. Wang, and G.-S. Xu, "Growth, characterization and properties of relaxor ferroelectric PMN-PT single crystals," *Ferroelectrics,* vol. 229, pp. 207-216, 1999.

[61] J. L. Hockel, A. Bur, T. Wu, K. P. Wetzlar, and G. P. Carman, "Electric field induced magnetization rotation in patterned Ni ring/Pb(Mg1/3Nb2/3)O-3]((120.32))-[PbTiO3](0.32) heterostructures," *Applied Physics Letters,* vol. 100, Jan 9 2012.

[62] S. Zhang, Y. G. Zhao, P. S. Li, J. J. Yang, S. Rizwan, J. X. Zhang*, et al.*, "Electric-field control of nonvolatile magnetization in Co40Fe40B20/Pb(Mg(1/3)Nb(2/3))(0.7)Ti(0.3)O3 structure at room temperature," *Phys Rev Lett,* vol. 108, p. 137203, Mar 30 2012.

[63] R. Streubel, P. Fischer, F. Kronast, V. P. Kravchuk, D. D. Sheka, Y. Gaididei*, et al.*, "Magnetism in curved geometries," *Journal of Physics D: Applied Physics,* vol. 49, p. 363001, 2016.

[64] R. D. McMichael and M. J. Donahue, "Head to head domain wall structures in thin magnetic strips," *Ieee Transactions on Magnetics,* vol. 33, pp. 4167-4169, Sep 1997.

[65] M. J. Donahue, *OOMMF user's guide [microform] / M.J. Donahue, D.G. Porter*. Gaithersburg, MD: U.S. Dept. of Commerce, Technology Administration, National Institute of Standards and Technology, 1999.

[66] J. H. Ha, R,. Kirschner, J. , "Micromagnetic study of magnetic configurations in submicron permalloy disks," *Physical Review B,* vol. 67, 2003.

[67] Y. Y. Huang and Y. M. Jin, "Phase field modeling of magnetization processes in growth twinned Terfenol-D crystals," *Applied Physics Letters,* vol. 93, p. 142504, 2008.

[68] E. Rapoport, D. Montana, and G. S. Beach, "Integrated capture, transport, and magneto-mechanical resonant sensing of superparamagnetic microbeads using magnetic domain walls," *Lab Chip,* vol. 12, pp. 4433-40, Nov 7 2012.